Physics of the Earth and Planetary Interiors 340 (2023) 107035

Contents lists available at ScienceDirect

Physics of the Earth and Planetary Interiors

journal homepage: www.elsevier.com/locate/pepi

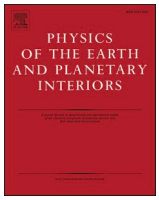

The mantle transition zone beneath eastern North America: Receiver functions and tomographic velocity models

Alexander L. Burky [a,*,1], Jessica C.E. Irving [b], Frederik J. Simons [a]

[a] Department of Geosciences, Princeton University, Princeton, NJ 08540, United States of America
[b] School of Earth Sciences, University of Bristol, Bristol, UK

ARTICLE INFO

Keywords:
Mantle transition zone
Receiver functions
Appalachian Mountains
Great Meteor hotspot
Laramide slab

ABSTRACT

The eastern continental margin of North America, despite being a passive margin at present, records a comprehensive tectonic history of both mountain building and rifting events. This record is punctuated by several igneous events, including those associated with the Great Meteor and Bermuda hotspots. To gain a better understanding of the state of the mantle beneath this region, we employ the massive quantity of seismic data recorded by the USArray to image the mantle transition zone beneath eastern North America. To construct these images, we first calculate *P*-to-*s* receiver functions using an iterative time-domain deconvolution algorithm. These receiver functions are then automatically filtered by their quality, using a set of rigorous criteria, and subsequently summed using common conversion point stacking. We present several cross sections through these stacks, which show remarkable features such as a thinned transition zone beneath the independently observed northern Appalachian and central Appalachian low-wavespeed anomalies, as well as a thickened transition zone beneath western Tennessee associated with the Laramide slab stagnating at depth. In addition to discussing these geologically relevant features, we perform a technical analysis of the effects of using various seismic velocity models for the moveout correction of our receiver functions. We find that the thickness of the mantle transition zone under eastern North America is a robust measurement, while the resolved depths of the 410 and 660 km discontinuities are model dependent.

1. Introduction

To acquaint the reader with the key events that have shaped the geologic history of eastern North America, we briefly review them here. A sensible starting point is the Appalachian orogeny, which occurred roughly 300 Ma during the collision of the African and North American continents (Hatcher et al., 2010). Around 230–200 Ma, the supercontinent of Pangaea broke up, causing eastern North America to rift apart from Africa (Brunsvik et al., 2021). By about 100 Ma, the Farallon slab was subducting beneath central North America (Sigloch, 2011), while the Great Meteor hotspot was active beneath New England (Kinney et al., 2021). Finally, at 50–30 Ma, magmatic activity in the region led to the formation of Bermuda and scattered basaltic volcanism in the central Appalachians (Mazza et al., 2014). When we consider all of these events, it makes sense that eastern North America warrants a special classification as a *volcanic* passive margin (Geoffroy, 2005).

In this work, we employ mantle transition zone (MTZ) receiver functions to map the depths to the 410 and 660 km discontinuities (hereafter referred to as 'the 410' and 'the 660') beneath eastern North America, as well as the MTZ thickness in the region. Evidence for a '520' is weak, yet widespread (Zhang et al., 2022). For a comprehensive review of mantle seismic discontinuities, see Deuss et al. (2013). Recent high-frequency global studies have revealed significant short-wavelength complexity at the base of the mantle transition zone (e.g., Wu et al., 2019; Mao et al., 2022). The recent gains in data coverage and the availability of multiple high-quality tomographic velocity models enable our present investigation into the structure of this dynamically important zone. Our high-resolution results are made possible by the dense spatial coverage of data provided by the USArray (Long et al., 2014).

Previous receiver function studies using USArray data have observed a variety of features in the MTZ beneath the eastern United States: notably, thickening beneath the Midwest from Iowa to Tennessee (Maguire et al., 2018) and moderate thinning beneath areas along the

* Corresponding author.
E-mail address: aburky@alumni.princeton.edu (A.L. Burky).
[1] Now at RPS Group, a Tetra Tech Company.

https://doi.org/10.1016/j.pepi.2023.107035
Received 3 June 2022; Received in revised form 21 February 2023; Accepted 26 April 2023
Available online 11 May 2023

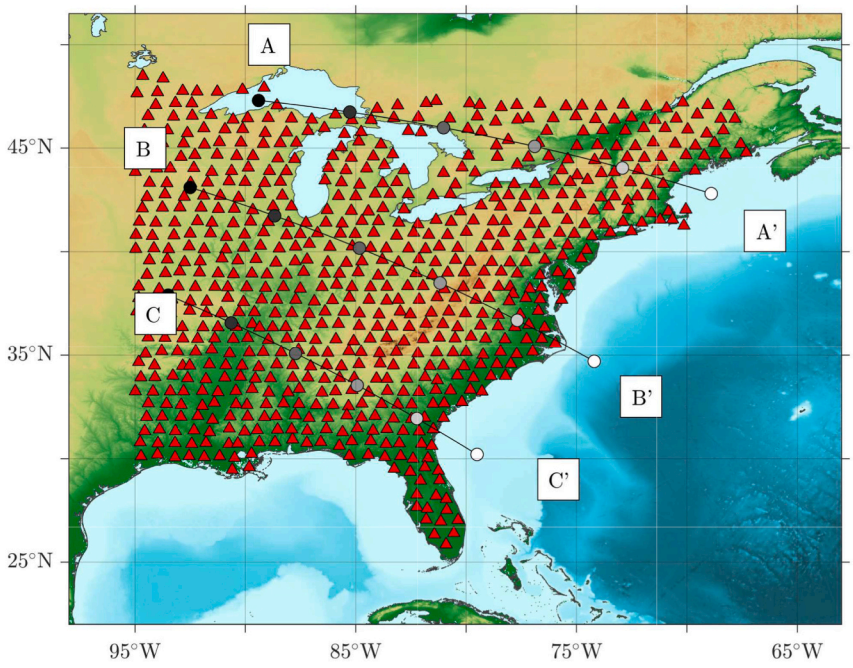

Fig. 1. Distribution of the USArray Transportable Array (TA) seismometers (red triangles) which contributed data to our study. Great-circle sections indicate cross sections A-A′, B-B′, and C-C′, which are discussed in the *Results*. The gray dots are intended to act as distance markers along the cross sections. The Great Meteor seamounts are near label A′, and the bathymetric swell surrounding Bermuda is east-southeast of label B′. See Supplementary Fig. S1 for an annotated map.

Atlantic coastal plain into the Appalachians (Keifer and Dueker, 2019). These observations agree with an earlier receiver function study which also identified thinning in the region beneath the central Appalachians and the adjacent Atlantic coastal plain (Li et al., 1998, their Fig. 3c).

In addition to receiver functions, work has been done using *SS* precursors to map the structure of the MTZ beneath North America. One difficulty with these studies is the reliance on favorable event-station geometries for *SS* bounce points, leading to poorer resolution than receiver functions beneath the USArray (Houser, 2016; Huang et al., 2019; Zhang et al., 2023). This problem has only recently begun to be remedied with methods that use near-station topside reverberations, such as *Ss*660*s*, which increase the range of usable geometries for precursor studies (Shearer and Buehler, 2019). Interestingly, the latter study also observed thickening of the MTZ beneath the Midwest, with a pronounced thickening below western Tennessee. The thinning beneath the Atlantic coastal plain, however, appears more modest in that study, though it lies at the edge of their resolvable region.

Adding to the complexity of our study area is the New Madrid Seismic Zone (NMSZ) beneath eastern Missouri and western Tennessee, which has been the host of several large earthquakes in recorded history (Page and Hough, 2014). MTZ studies have identified significant thickening beneath the NMSZ, but no link has been established between these two features (Gao and Liu, 2014). This thickening has, however, been attributed to a stagnant portion of the Farallon slab, referred to as the Laramide slab, which today resides in the MTZ (Sigloch, 2011). This feature has been consistently resolved in a *P* wave travel-time tomography study (Wang et al., 2019), and a joint *P* and *S* wave travel-time tomography study (Savage, 2021).

1.1. The Northern Appalachian Anomaly

In the northeastern United States, seismic studies have revealed the presence of a strong, localized, low-velocity anomaly, which has been hypothesized to be an indication of geologically recent asthenospheric upwelling 100 to 300 km beneath New England (Menke et al., 2016; Levin et al., 2018). This feature has been referred to as the Northern Appalachian Anomaly (NAA). Geographically coincident with this feature is the track of the Great Meteor hotspot (Morgan, 1971), which is thought to have underlain the region from ∼140 to 100 Ma (Kinney et al., 2021), but now underlies the Atlantis-Meteor Seamounts (Sleep, 1990) east of the Mid-Atlantic Ridge. Attributing the present-day seismic velocity anomalies to this long gone hotspot appears contradictory, and has encouraged authors to propose alternative scenarios such as edge-driven convection (King and Anderson, 1998), or lithospheric delamination after the Appalachian orogeny some 300 Ma (Nelson, 1992; Levin et al., 2000).

A geochemical study by Torgersen et al. (1995) measured excess ^{3}He in groundwater in New Hampshire. Their observations were suggestive of geologically recent contamination by a reservoir containing primordial mantle helium, which is typical of volcanically active regions such as ocean islands (Jackson et al., 2017)—not of geologically old and quiescent regions like the northeastern United States. One possible explanation for this particular signature is that it may be a remnant of the extensive White Mountain plutonism (190–90 Ma) associated with the passage of the Great Meteor plume.

Deeper into the mantle, several recent tomography models have imaged low-velocity anomalies extending through the MTZ beneath the northeastern United States. Sigloch (2011) refers to these features as the "slow blanket" above the old Farallon slab, owing to their location directly above an eastward dipping high-velocity feature beneath the Midwest and eastern North America. A more recent tomography study by Savage (2021) also imaged low V_P and V_S anomalies extending through the MTZ beneath this region. The appearance of these anomalies directly above the old Farallon slab is not likely to be a coincidence, and some authors have speculated it may be the signature of a deep dewatering phenomenon (van der Lee et al., 2008).

1.2. The Central Appalachian Anomaly

Toward the south, the presence of a roughly linear seismic low-velocity anomaly in the lower lithosphere extending from Missouri to Virginia has been interpreted as a previously undetected hotspot track

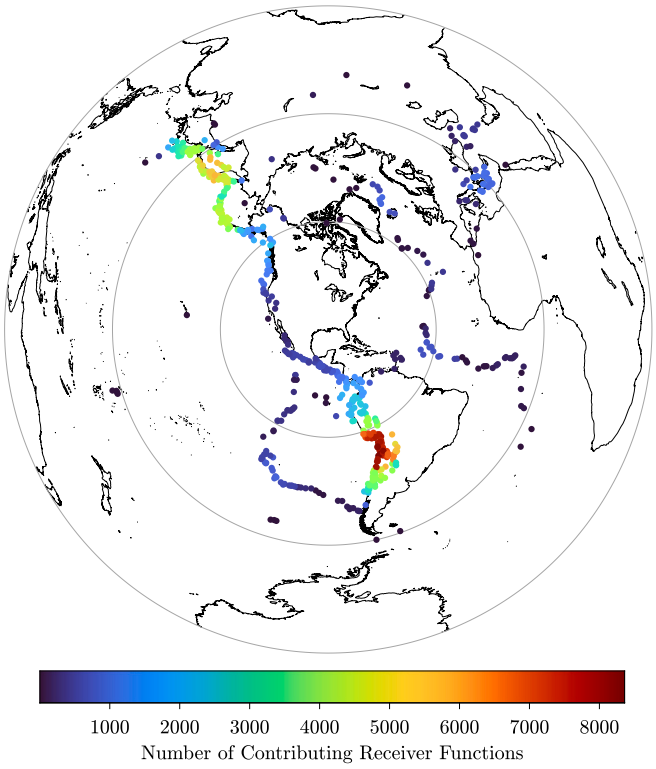

Fig. 2. Distribution of the events contributing to the 40,571 high-quality receiver functions used in this study. Each colored dot represents the total number of accepted receiver functions within a $2^\circ \times 2^\circ$ area around a given event. Concentric gray circles are evenly spaced at distances of 45°, up to a maximum of 135° from the center of the array. Most of our data come from events along the Pacific Ring of Fire, but there are additional contributions from the Mid-Atlantic Ridge and the eastern Mediterranean. Also note that there is considerably more data from distances between 45° and 90° from the center of the array, as events within this distance range are recorded by the majority of stations used in our analysis. Supplementary Fig. S5 shows the depths of these events.

(Chu et al., 2013). This theory is reinforced by the presence of 75-Myr-old diamondiferous kimberlites in Kentucky (Agee et al., 1982), thought to be sourced from a deep mantle reservoir. The timing of these events, however, is inconsistent with Eocene (~47 Ma) basaltic volcanism in this same region (Mazza et al., 2014). This second event is temporally coincident with offshore magmatic activity which led to the formation of Bermuda and its associated large bathymetric swell (Vogt and Jung, 2007), whose origin remains ambiguous (Burky et al., 2021b) due to the lack of an associated hotspot track and geochemical signatures (Mazza et al., 2019).

A study of seismic anisotropy in this region observed null splitting near the Atlantic coast, which the authors interpreted as due to vertical flow induced by the impinging Farallon slab (Long et al., 2010). These observations are compounded by the presence of high attenuation in the asthenosphere beneath the area, ascribed to upwelling asthenosphere and the possible presence of melt (Byrnes et al., 2019). Seismic tomography models consistently resolve a low-velocity anomaly extending through the upper mantle beneath this region at present (e.g. Simmons et al., 2010, 2012; Schaeffer and Lebedev, 2014; Lei et al., 2020), alluding once again to the presence of a long-gone hotspot. These low-velocity anomalies are so persistent in tomography models that they have been referred to as the Central Appalachian Anomaly (CAA) (Schmandt and Lin, 2014).

2. Data & modeling

Our main data type in this work is the *P*-to-*s* conversion of teleseismic earthquake waves at discontinuities in the mantle. To isolate these converted phases, we first requested three-component seismograms recorded by a subset of USArray stations (network code TA, for Transportable Array) for all earthquakes with a moment magnitude $M_w > 5.5$ and within an epicentral distance $35^\circ \leq \Delta \leq 90^\circ$ of the station (Fig. 1). This resulted in 1995 events recorded by 702 stations. We then removed the mean and linear trend from each record, and corrected for the instrument response, converting our seismograms from digital counts to velocity (m/s) using the methods outlined by Burky et al. (2021a). Before any subsequent processing, we bandpassed all seismograms between 0.02 and 0.2 Hz using a third-order Butterworth filter. Each record was then cut 30 s before and 90 s after the theoretical *P*-wave arrival time calculated in one-dimensional (1-D) seismic velocity model *iasp91* (Kennett and Engdahl, 1991), to create a record containing only the *P* wave and its coda. To maximize *P*-to-*s* converted energy, we rotated the horizontal components from the north and east (NE) orientation to the radial and transverse (RT) orientation.

After performing these preliminary processing steps, we calculated receiver functions by deconvolving the vertical (Z) from the radial (R) component using the iterative time domain deconvolution algorithm of Ligorra and Ammon (1999), as described and implemented by Burky et al. (2021b). This resulted in 173,801 radial receiver functions. Since we are not focused on investigating anisotropy in this work, we did not compute transverse receiver functions, and our results do not inform us of any differences between V_{SV} and V_{SH} in the study region. Before continuing with any analysis, we performed an automated quality control of these receiver functions. The four parameters that we calculate for each receiver function are, (1) the Z component signal-to-noise ratio (SNR), (2) the R component SNR, (3) the quality of fit calculated after the iterative time domain deconvolution, and (4) a receiver function quality factor, ν, quantifying the shape of the resulting receiver function (for further details about these four parameters, see Burky et al., 2021b). We accepted receiver functions with SNR values greater than 2, quality of fit greater than 80%, and ν greater than 0.1. After this step, 40,571 receiver functions remained (see Fig. 2 for the geographic distribution of the accepted receiver functions). Although our dataset shows a geographic bias in terms of the distribution of events, this does not influence any of our interpretations due to the extremely dense station coverage provided by the USArray (see Fig. 3).

3. Methods

In order to meaningfully analyze and interpret our receiver functions, we performed additional processing steps to resolve the mantle transition zone discontinuities that we are concerned with imaging. The first of these steps is the moveout correction of our data, allowing us to go from the time domain to the depth domain via a seismic velocity model. Then, using these depth-domain receiver functions, we can produce images of the desired discontinuities by utilizing stacking techniques. These stacks can then be visualized and analyzed to construct maps of the MTZ properties across our study region.

3.1. Time to depth conversion

To accomplish our first task of depth converting the receiver functions, we make use of the following time to depth conversion formula (Chevrot et al., 1999):

$$t_{Pds}(p,Z) = \int_0^Z \left[\sqrt{V_S^{-2}(z) - p^2 r^{-2}} - \sqrt{V_P^{-2}(z) - p^2 r^{-2}} \right] dz, \quad (1)$$

where $t_{Pds}(p,Z)$ is the time in the receiver function corresponding to a conversion from a particular depth, Z, in a seismic velocity model with P

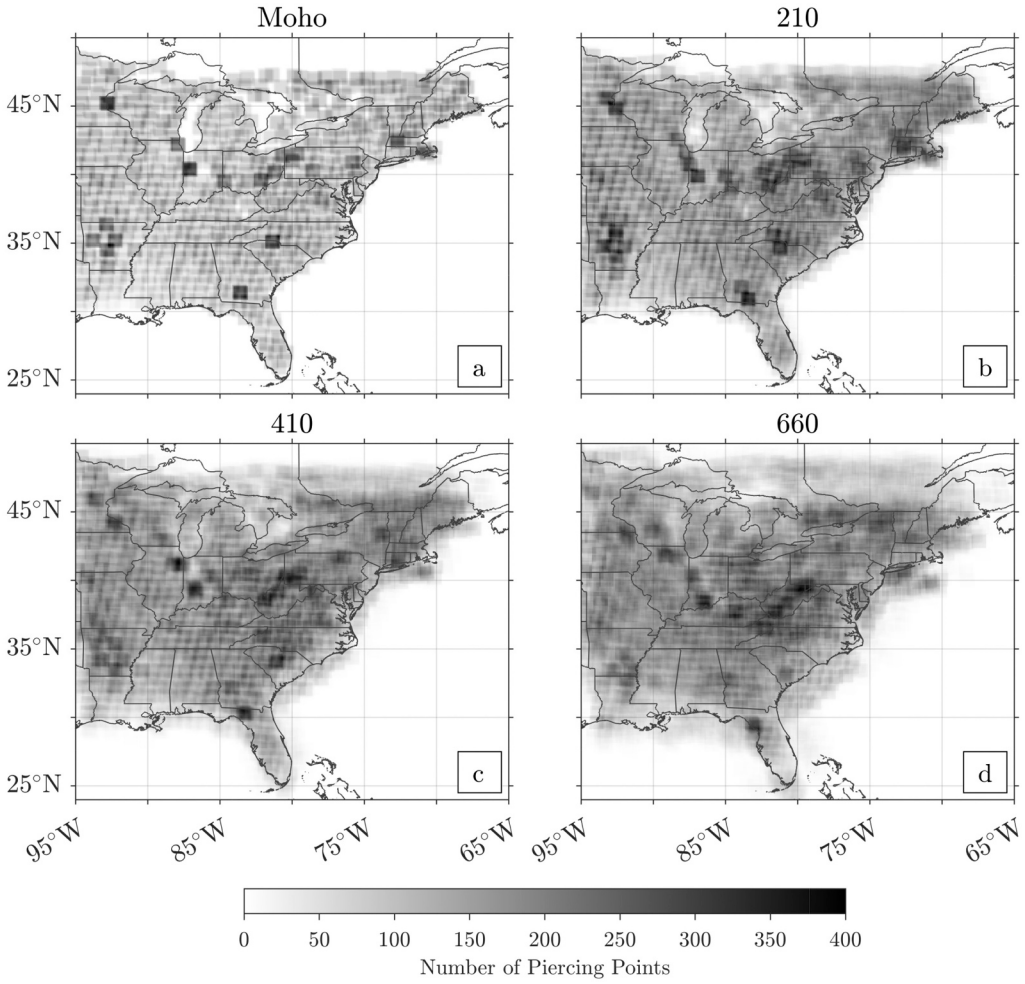

Fig. 3. Density of receiver functions contributing to $1^\circ \times 1^\circ$ cells at four mantle depths ('Moho' corresponds to 35 km). Ray coverage is fairly uniform throughout the mantle transition zone, but is biased by the locations of stations at shallower depths. Bins with anomalously high densities of contributing receiver functions can be attributed to exceptional data quality at certain stations, combined with the somewhat uneven spacing of the US Array stations. See Supplementary Fig. S6 for station density.

and S wave speeds as a function of depth z, given by $V_P(z)$ and $V_S(z)$, p is the P-wave ray parameter (s/km) of the particular event-station pair, and $r \in [0, 1]$ is the ratio of the discontinuity radius, $R_\oplus - Z$, to the Earth's radius, $R_\oplus$. We compute this integral in six different velocity models, using a depth increment of $\Delta z = 0.1$ km.

The first model which we used to perform time-to-depth conversion was 1-D reference model *iasp91* (Kennett and Engdahl, 1991). Next, we used a hybrid 1-D/3-D model made by replacing the crust in *iasp91* by the 3-D global crustal velocity model CRUST1.0 (Laske et al., 2013). Lastly, we used four different 3-D tomography models. Three of these models are global models: GyPSuM (Simmons et al., 2010), LLNL_G3D_JPS (Simmons et al., 2012), and GLADM25 (Lei et al., 2020), and the fourth model is a regional model of North America, SL2013NA (Schaeffer and Lebedev, 2014). We selected these four tomography models because they span a range of model construction philosophies, have different sampling densities, and are publicly available, user-friendly models containing absolute P- and S-wave velocities in our study region. We recognize that there are many more tomography models to choose from that could be used to perform the time-to-depth conversion, not to mention additional complexity such as wavespeed anisotropy (Chang et al., 2014). The open-source software that we developed for our study lends itself to reuse by other authors wishing to investigate the effects of additional tomographic models.

To highlight the properties of the four selected tomographic models, we briefly review them here. Model GyPSuM is constructed largely from body-wave data (P- and S-wave traveltimes), with the addition of gravity, plate motion, dynamic topography, core-mantle boundary ellipticity, and mineral physics parameters. Model LLNL_G3D_JPS builds on GyPSuM with additional body-wave traveltime measurements, and a more densely spaced model parameterization. In contrast, global model GLADM25 uses a full-waveform approach on much longer-period data (down to 17 s) to constrain P- and S-wave velocities in a transversely isotropic model. Lastly, regional model SL2013NA inverts surface and S-waveform data to constrain perturbations in P and S velocity and S-wave azimuthal anisotropy with respect to a reference model based on Crust2.0 (Bassin et al., 2000) and *ak135* (Kennett et al., 1995). All four selected models contain crustal heterogeneity; however, global model GyPSuM has such low resolution in the crust (on the order of 5°) that it does not effectively capture small scale features.

In order to use the integral in Eq. (1) with these 3-D models, we used the ray-tracing tool of model LLNL_G3D_JPS to compute P-wave ray-paths through that model to find the paths corresponding to each event-station pair in our dataset. We used these paths for the remaining 3-D models, and we used P-wave paths calculated using the TauP Toolkit (Crotwell et al., 1999) for 1-D model *iasp91* and the hybrid model that includes CRUST1.0. All of the models were then queried along these respective raytraced paths to construct the necessary velocity profiles, $V_P(z)$ and $V_S(z)$. It is also worth noting that in our time-to-depth conversion process we are not accounting for any effects of anisotropy on V_S. The models we are using to depth-convert our receiver functions have isotropic S-wave velocities, so a deviation in V_{SV} from these velocities would lead to a shift in the absolute depths of discontinuities resolved with this method. Irrespective of this limitation, as we will show in our *Results* and *Discussion* sections, the resolved absolute depths of MTZ discontinuities are highly model dependent, while the MTZ thickness is shown to be robust. Since radial anisotropy is most

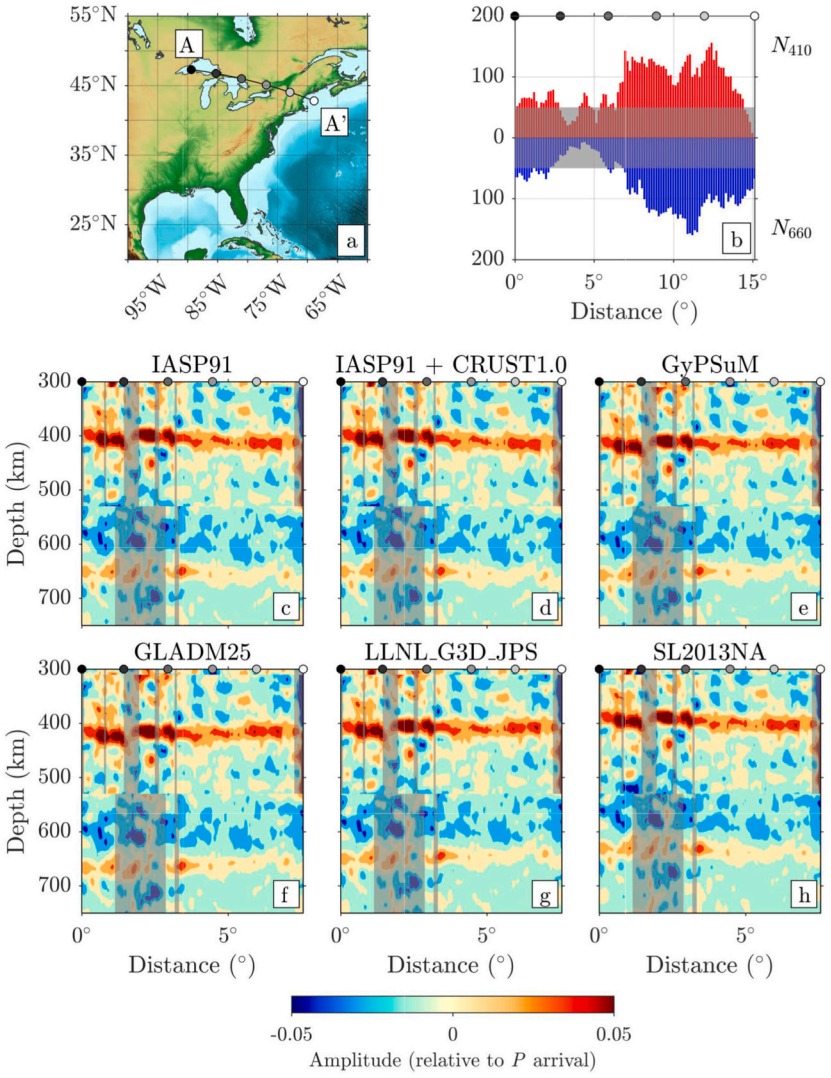

Fig. 4. Mantle transition zone (MTZ) structure in the region of the Northern Appalachian Anomaly (NAA). (a) Map showing the location of the cross section. (b) Histogram showing the number of receiver functions contributing to the 410 (red) and 660 (blue) portions in the cross section. Data quantity tapers off near the Great Lakes and into Canada. (c-h) Cross sections through common conversion point (CCP) stacks in six different tomographic velocity models described in *Methods*. Bins with fewer than 50 receiver functions are covered with a transparent gray box, corresponding to the grayed-out region of panel (b). Note the relative thinning of the MTZ from NW to SE along this cross section, coincident with the location of the NAA.

significant at shallow depths and near subduction zones, and less significant within the MTZ (e.g. Chang et al., 2015; Simmons et al., 2021), we ignore its effects here.

3.2. Common conversion point stacking

The dense geographic distribution of stations in our dataset allowed us to employ array processing techniques to robustly construct high-resolution images of the MTZ beneath eastern North America. Specifically, we produced common conversion point (CCP) stacks of our data, inspired by the method outlined by Dueker and Sheehan (1997). The data density for our CCP stacks is shown in Fig. 3. Our data coverage in the mantle transition zone is fairly consistent over the entire study region, and the majority of bins beneath the continent contain at least 100 receiver functions.

First, we calculated theoretical raypaths through 1-D model *iasp91* for all of our event-station pairs using the TauP Toolkit. Next, we constructed a grid containing the latitude range 22.5°N to 51.5°N, and the longitude range 98.5°W to 63.5°W, with a $1^\circ \times 1^\circ$ cell size. We then found where the computed raypaths pierced our grid at depths 35, 210, 410 and 660 km. Depth-converted receiver functions corresponding to each of these rays were then stacked together with the other rays which were contained in the $1^\circ \times 1^\circ$ cell, to create a volume where the center of each cell contained a CCP-stacked receiver function. The entire grid was then shifted sequentially by increments of 0.1°, and the stacking was repeated, until the grid had been shifted by 1°. This resulted in a volume with CCP stacks of $1^\circ \times 1^\circ$ stacking width on a grid of resolution $0.1^\circ \times 0.1^\circ$. Finally, the CCP volumes containing each of our four chosen piercing depths (35 km, 210 km, 410 km, and 660 km) were stitched together to construct our final CCP volume, where the depth range 0—120 km corresponds to the 35 km stack, 120—300 km corresponds to the 210 km stack, 300—530 km to the 410 km stack, and 530—750 km to the 660 km stack (the stitched joins can be seen in the cross-section slices shown in Figs. 4–6).

4. Results

After computing the common conversion point stacks as described above, we have at our disposal a collection of six different images of the mantle transition zone beneath eastern North America. Using these stacks, we can seek answers to two important questions: first, what is the effect of the choice of seismic velocity model on the resulting image? And second, are there specific features of the MTZ discontinuity structure which are clearly and commonly resolved in each of our CCP stacks?

In an effort to answer the first question, we start by visually comparing a sequence of cross sections taken through each of our CCP stacks. Selected cross sections can be found in Figs. 4, 5, and 6. The first point to note is that we clearly resolve both the 410 and 660 in each of

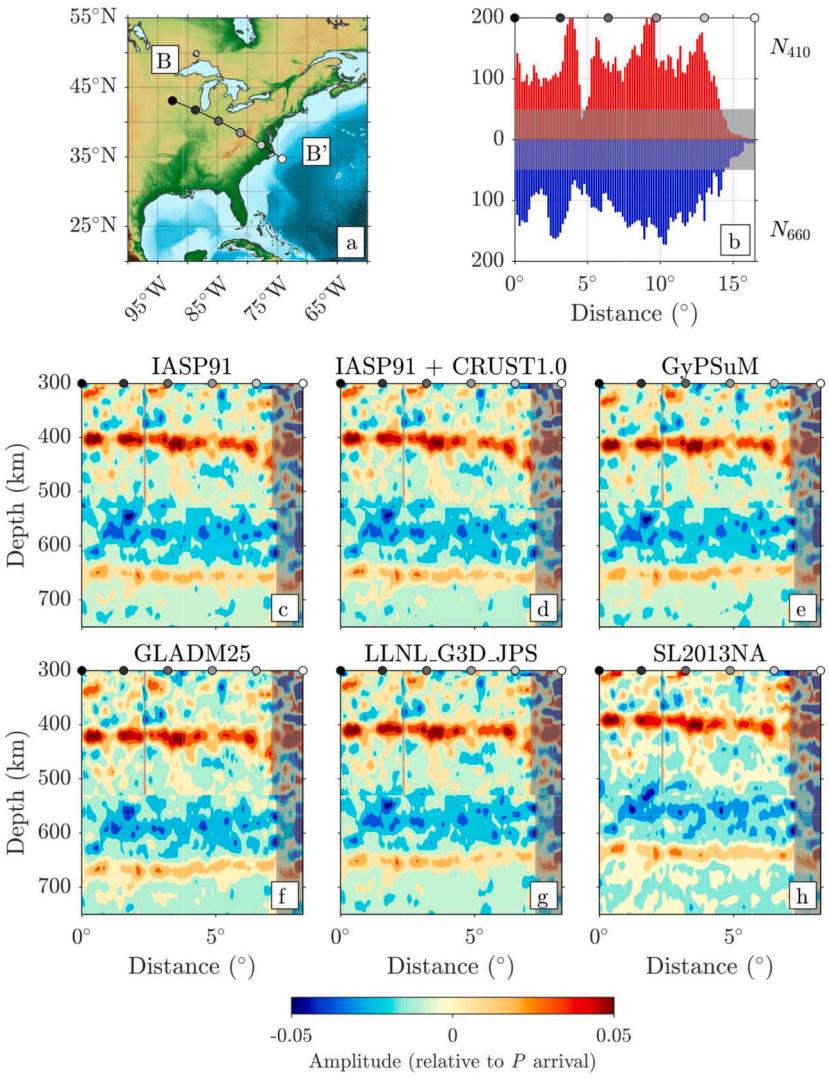

Fig. 5. Mantle transition zone (MTZ) structure in the region of the Central Appalachian Anomaly (CAA), laid out as Fig. 4. Note the considerable amount of topography on the 410 discontinuity, and the strong thinning of the MTZ at the SE end of the cross section. Also note the data sparsity and poor resolution at the southeasternmost end of this cross section. The negative-polarity signals around 600 km depth (also present in Figs. 4 and 6), despite having a similar magnitude to *P660s*, are most likely artifacts from filtering (see Supplementary Fig. S7) and the presence of the *PcP* phase.

these cross sections, regardless of the velocity model used to moveout-correct our receiver functions. Second, the average amplitude of the 410 signal tends to be higher than that of the 660 signal (see Supplementary Fig. S11). This difference could indicate that the magnitude of the *S*-wave velocity contrast at the 660 is weaker than that at the 410. A thorough investigation quantifying the magnitude of this difference is beyond the scope of this study and may require consideration of full-waveform effects (Zhang et al., 2023). Another factor leading to this amplitude difference could be due to the fact that the time-depth conversion, Eq. (1), becomes less accurate for converted waves at this depth, as can be seen by the slightly underestimated depth of the 660 (see Fig. S7), leading to less constructive stacking of signals from the 660. The third result to note is that each of the selected cross sections displays a considerable amount of topography on the MTZ discontinuities, as we explore more fully below. Finally, the resulting images seem to resolve consistent features regardless of the velocity model used, but with relative shifts in the depths of the discontinuities. These discrepancies are likely due to the differences in model construction (data types, inversion methods) described above, leading to a range of *Pds* moveouts across different models.

To further explore this final point, we performed pairwise cross correlations between each of our CCP stacks, in an effort to see how consistent the resolved features were. We found that our stacks were strongly correlated with one another (correlation coefficient $\rho > 0.9$) with relative shifts of about 10–20 km. Animations showing these cross correlations across the entire CCP volume can be found in the Supplementary Materials, and stills from these animations are included as Supplementary Figs. S15–S21 To our knowledge, this is the first analysis of the pairwise cross correlations of a suite of CCP stacked receiver functions. These animations show that the choice of velocity model used in depth converting receiver functions can lead to large variations in the resulting depths of the 410 and 660. However, these variations tend to shift both discontinuities in the same direction, implying that the measured thickness of the mantle transition zone is less sensitive to the choice of velocity model.

To help illustrate this point, as well as to explore the geographic variations in MTZ discontinuity structure, we made maps showing the depths of the 410 and 660, as well as the measured MTZ thickness, in all of our 3-D corrected CCP stacks (see Fig. 7). In these maps, we can see that model GLADM25 tends to shift the 410 and 660 to greater depths, while model SL2013NA tends to shift them to shallower depths. Models GyPSuM and LLNL_G3-D_JPS show less exaggerated shifts of the discontinuities away from 410 and 660 km. All four models, however, show a relatively thinned region east of the Appalachians, compared to the global average of 242 km (Lawrence and Shearer, 2006), and a relatively thickened region to the west of the Appalachians. Of particular interest are two roughly linear thinned zones which trend NW-SE. These thinned zones correspond to cross sections A-A′, B-B′ (see Figs. 4 and 5). In addition, a thickened region beneath western Tennessee is manifest in cross section C-C′ (see Fig. 6).

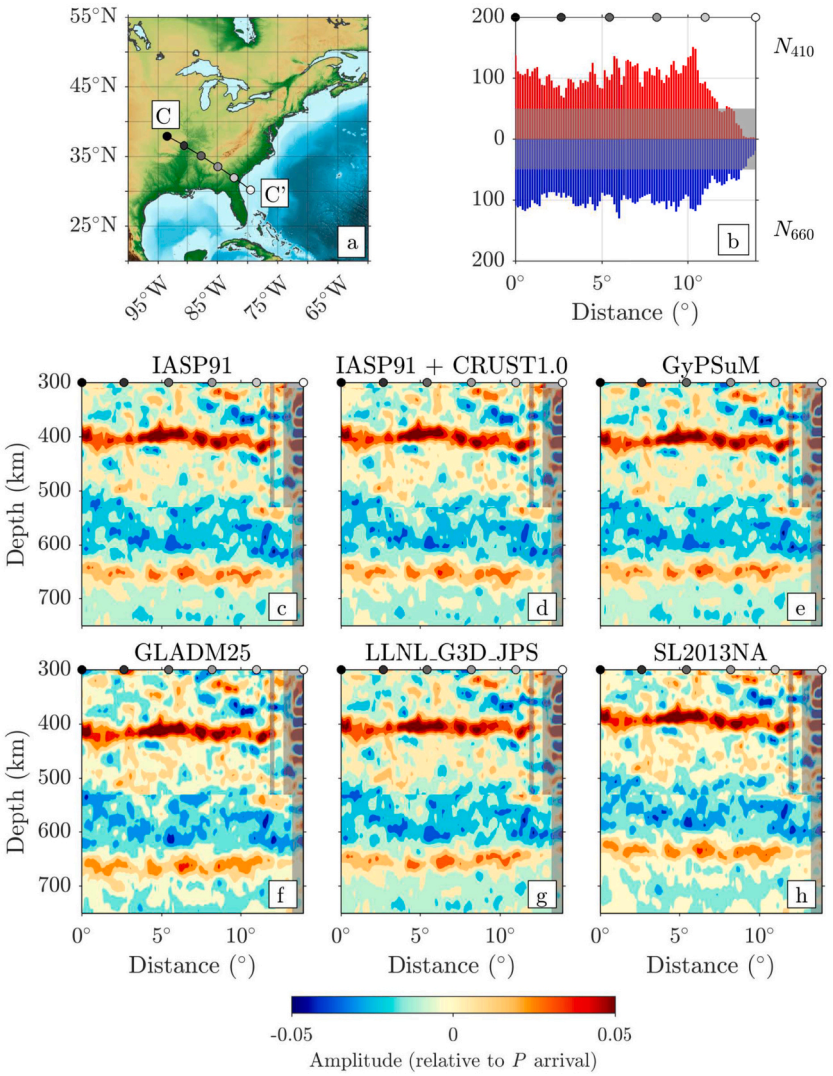

Fig. 6. Mantle transition zone (MTZ) structure in the region of the Southern Appalachian Anomaly, laid out as Fig. 4. Note again the strong topography on the 410 and 660 discontinuities. This cross section shows significant thickening of the MTZ at the western end of the cross section, beneath western Tennessee. Data coverage is fairly uniform, with resolution tapering off at the southeasternmost end of this cross section.

5. Discussion

5.1. The importance of 3-D moveout corrections

We have shown that the choice of seismic velocity model has a considerable effect on the apparent depth of the MTZ discontinuities. In the most extreme case, an average discrepancy of 21.6 km in the apparent depth of the 410 and an average discrepancy of 26.1 km in the apparent depth of the 660 were found between CCP stacks made using models GLADM25 and SL2013NA (see Supplementary Figs. S9 and S10). These discrepancies are contrasted by an average difference of 4.4 km between the apparent MTZ thicknesses found in these stacks (see Fig. 8). This highlights that the apparent depths of the 410 and the 660 can be difficult to accurately constrain using receiver functions, even after performing 3-D depth corrections. Fortunately, the MTZ thickness is much more consistently resolved regardless of the seismic velocity model used to depth-convert receiver functions. Consequently, this is the feature which we will frame our discussion on, and we suggest that future MTZ receiver function studies follow this example.

In an effort to explore and understand the mechanism leading to these discrepancies, we performed an analysis of the time-to-depth conversion integral in Eq. (1) for each of the 3-D velocity models used in our study. The results of this analysis are summarized in Supplementary Fig. S8. We found that the *Pds* conversion depth associated with a particular time in a receiver function varied considerably from the outset in each of the 3-D models. For times in the range of 0 to 10 s after the *P* arrival in the receiver function, there is a spread in possible conversion depths of roughly 4 km. This would lead to relative discrepancies in apparent Moho depths on the order of 4 km. At times greater than 20 s, this discrepancy has grown to roughly 20 km, as can be seen in our results. The slopes of these curves, however, remain roughly constant through the times associated with MTZ *Pds* arrivals, which leads to the decreased variability in our observed MTZ thicknesses using different tomographic models.

5.2. The Northern Appalachian Anomaly

In light of the previous discussion, we are confident that the observed MTZ thinning in our CCP stacks is a robust feature. This leads to interesting implications for the NAA, which had only been observed at shallower asthenospheric depths of 100 to 300 km (Menke et al., 2016; Levin et al., 2018). We suggest that this feature extends deeper than previously known, and may be associated with a surviving hot thermal anomaly beneath New England. See Supplementary Fig. S12 for cross

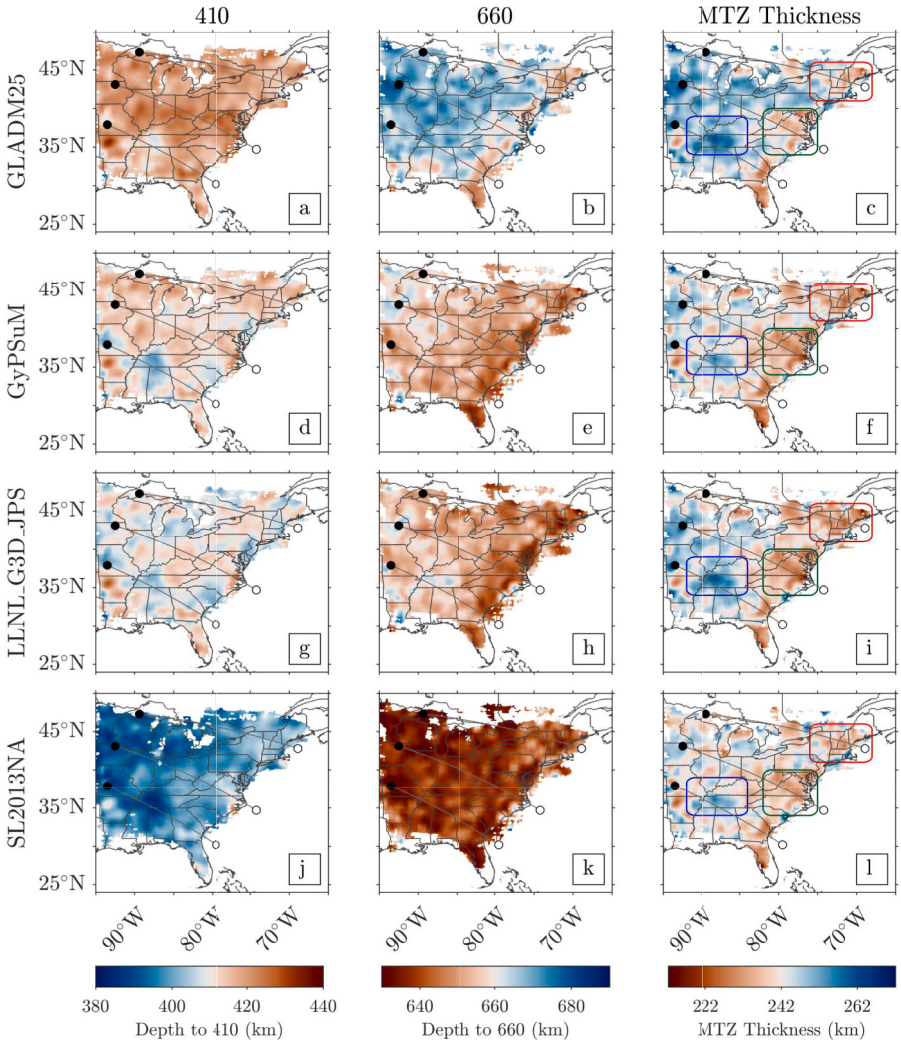

Fig. 7. Measured 410 and 660 depth, and MTZ thickness, for CCP stacks made using four different 3-D velocity models for the depth conversion of our receiver functions: (a-c) GLADM25, (d-f) GyPSuM, (g-i) LLNL_G3-D_JPS, and (j-l) SL2013NA. Only locations with 50 or more receiver functions are shown. Note that models GLADM25 and SL2013NA differ markedly in the depths of the 410 and 660, while GyPSuM and LLNL_G3-D_JPS seem more consistent with one another. Also note that all four models are fairly consistent in their resolved MTZ thickness. The thinned zones shown in cross sections A-A′, B-B′, and C-C′ (Figs. 4, 5, and 6) are also apparent in all four models. Red, green, and blue inset boxes denote the approximate locations of the NAA, CAA, and Laramide slab anomaly, respectively.

sections through the four tomographic velocity models.

We can estimate the magnitude of this thermal anomaly using the following relation from Helffrich (2000):

$$z = z_0 + \delta T \left(\frac{dz}{dP}\right) \left[\left(\frac{dP}{dT}\right)_{660} - \left(\frac{dP}{dT}\right)_{410} \right], \quad (2)$$

where z represents the observed MTZ thickness, $(dP/dT)_{660}$ and $(dP/dT)_{410}$ are the Clapeyron slopes of the ringwoodite to bridgmanite and magnesiowüstite (ferropericlase) phase transition, and the olivine to wadsleyite phase transition, respectively. We use a value of $z_0 = 242$ km (Lawrence and Shearer, 2006) for the global average MTZ thickness, and values of $(dP/dT)_{660} = -2.6$ MPa/K and $(dP/dT)_{410} = 3.1$ MPa/K (Akaogi et al., 2007) for the Clapeyron slopes. In reality, the Clapeyron slopes of these phase transitions are somewhat variable, ranging from −0.2 to −3.6 MPa/K for $(dP/dT)_{660}$ (e.g., Kojitani et al., 2016; Muir et al., 2021), and 1.8 to 4.0 MPa/K for $(dP/dT)_{410}$ (e.g., Yu et al., 2008) due to both experimental uncertainty and the degree of hydration of the mineral assemblage. However, since $(dP/dT)_{660}$ is negative and $(dP/dT)_{410}$ is positive, the association of a thin transition zone with a positive thermal anomaly holds true. To simplify the following discussion, we will quote temperature anomalies calculated using the aforementioned Clapeyron slopes, but the reader should keep in mind that these estimated anomalies could vary by roughly one order of magnitude with the choice of alternative Clapeyron slope values.

Using our four different CCP stacks, we can estimate bounds on the thermal anomaly associated with the NAA. The minimum MTZ thickness observed in our four models is 223 km (model LLNL_G3-D_JPS, beneath southern New Hampshire), but there is a range of 6 km in this measurement across the models (229 km for model GLADM25, see Supplementary Fig. S2 and Table S1). Inserting these values into Eq. (2) gives a range for the maximum thermal anomaly of ~89–130 K relative to global average MTZ temperature. To investigate the significance of this anomaly, we report statistics of the NAA sub-region relative to our entire dataset (see Table S1). We found that the average MTZ thickness within the NAA was between 235 and 238 km for the four models we tested, corresponding to a modest, positive (warm) thermal anomaly of ~27–48 K relative to the global average (Eq. 2). This thickness is roughly one standard deviation thinner than the average for our entire dataset.

Previous receiver function research on the MTZ beneath the NAA reported no evidence of thinning or deflection of the discontinuities (Li et al., 1998, their Fig. 3c), despite finding modest thinning beneath the central Appalachians and the adjacent Atlantic coastal plain. This has led recent work to suggest that this feature does not penetrate through the MTZ, and is instead confined to the shallow asthenosphere at depths less than 400 km (Menke et al., 2016). Our findings do not invalidate this previous work, but instead build upon it by suggesting that the NAA may weakly penetrate the MTZ below. In fact, if we consider the MTZ to be the lowermost extent of a shallow edge-driven convective cell, the observations of W-E aligned anisotropy can be interpreted as the horizontal flow associated with the bottom of such a cell (Long et al., 2016;

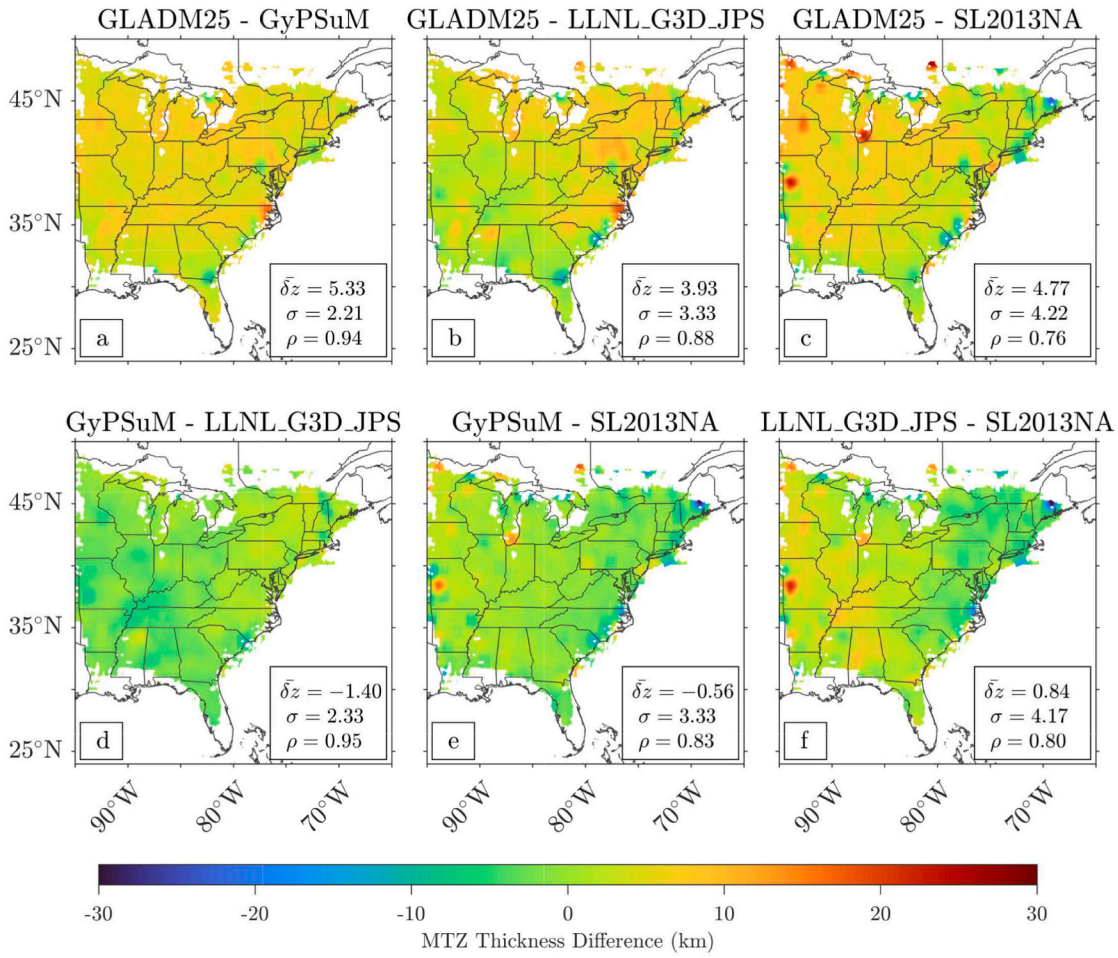

Fig. 8. Maps showing the differences between pairs of each of the MTZ thickness maps in Fig. 7. The legends report $\bar{\delta z}$, the mean value of the difference, σ, the standard deviation of the difference, and ρ, the correlation coefficient between the two maps. Note that the differences in thickness are on the order of a few km, and that the maps tend to be well correlated ($\rho > 0.7$). For similar maps showing the differences for the 410 and the 660, see Supplementary Figs. S9 and S10.

Levin et al., 2018). This could reconcile the puzzling observations of null splitting and W-E anisotropy beneath the NAA which stand as outliers to the rest of northeastern North America.

5.3. The Central Appalachian Anomaly

We can apply a similar analysis to the anomalously thin MTZ corresponding to the CAA to get an estimate of the magnitude of its thermal signature. See Supplementary Fig. S13 for cross sections through the tomographic velocity models.

The *minimum* MTZ thickness we observe is 214 km (model LLNL_G3D_JPS beneath the North Carolina-Virginia border), but there is a range of 14 km across the four models (228 km in models GLADM25 and SL2013NA, see Supplementary Fig. S3, and Table S1). This yields a range of ∼96–192 K for the *maximum* thermal anomaly relative to global average MTZ temperature. When we instead consider the *average* MTZ thickness within the CAA, we find that it is of similar thickness to the NAA, between 236 and 238 km, corresponding to an *average* thermal anomaly of ∼27–42 K relative to the global average.

When we consider all of the information presented so far, the CAA and NAA seem to be very similar in terms of their observed features. Both locations have a record of igneous activity, Eocene (∼ 47 Ma) volcanism in the area of the CAA (Mazza et al., 2014), and Cretaceous (∼ 140 to 100 Ma) volcanism in the area of the NAA (Kinney et al., 2021), and the present-day MTZ anomalies are of nearly identical magnitudes. We suggest that both of these features may be associated with small-scale convective cells generated by the contrast with the nearby Farallon slab remnants and continental craton. These cells seem to be long-lived, and may have been present during the passage of both the Great Meteor and Bermuda hotspots, providing them with the additional heat and buoyancy required to initiate active volcanism and plutonism. This interpretation is consistent with null splitting observations in both regions (Long et al., 2016), and with an edge-driven convection model (King and Anderson, 1998). With the passage of another transient heat source these regions might become active once again.

5.4. MTZ thickening associated with the Laramide slab

In addition to resolving regions of thinned MTZ beneath the NAA and CAA, we observe modest topography and thickening of the MTZ west of the Appalachians. Of particular note is a significantly thickened patch beneath western Tennessee, which we argue is associated with the stagnant Laramide slab. The Laramide slab is not an entire, distinct slab, but is rather the expression of a period of shallow-angle subduction of the Farallon slab which occurred 80 to 60 Ma (Humphreys et al., 2015). This shallow subduction was terminated by a break-off at depth and a westward migration of the trench around 50 Ma (Sigloch et al., 2008), leaving the shallowly subducting slab stalled in the transition zone. Recent tomographic images support this interpretation, showing evidence of shallow (< 700 km) seismically fast anomalies in the transition

zone beneath the Midwest (Sigloch, 2011). In the model of Sigloch (2011), these anomalies are greatest in the MTZ beneath western Tennessee, consistent with our observations of maximum thickening there. See Supplementary Fig. S14 for tomographic cross sections.

To quantify the magnitude of the thermal anomaly associated with this relict slab, we measure the maximum MTZ thickness beneath this region (see Supplementary Fig. S4 and Table S1). We observe a *maximum* MTZ thickness of 263 km (beneath western Tennessee in model GLADM25), and a range of 6 km for the maximum thickness (257 km in models GyPSuM and SL2013NA). These values correspond to a range of about −103 K to −144 K for the strongest cold thermal anomaly relative to global average MTZ temperature. When we instead consider the *average* MTZ thickness within this anomaly, we find that it spans a range of 245 to 249 km, and corresponds to an *average* thermal anomaly of about −21 K to −48 K relative to the global average. These anomalies are smaller than those observed beneath active subduction zones at present (van Stiphout et al., 2019), but this is not surprising considering how long the Laramide slab has been stalled in the MTZ.

5.5. Synthesis with previously published results

As was stated in the *Introduction*, eastern North America is aptly classified as a *volcanic* passive margin (Geoffroy, 2005). Our results reinforce this classification by demonstrating the plausability of hot thermal anomalies in the MTZ beneath the northern and central Appalachian mountains. This result also agrees with the recent receiver function work by Keifer and Dueker (2019), who found similar thinning beneath the Appalachians, as well as thickening beneath western Tennesee. The agreement between our studies is particularly encouraging since for the migration of their receiver functions they used two entirely different tomography models (Schmandt and Lin, 2014; Golos et al., 2018) than the four we investigated here. Interestingly, the magnitudes of the temperature anomalies they inferred, on the order of ±300 K to ±600 K, were even larger than the ones we measured, further emphasizing that the MTZ beneath this region is anything but average. Circling back to the *Introduction*, our results show that despite the lack of any modern volcanism, the perplexing presence of "hot-spot" signatures such as excess ^{3}He in the groundwater in New Hampshire (Torgersen et al., 1995) can be seen as the dying breaths of the region's volcanic legacy. The combination of an incoming slab from the west, the possibility of edge-driven convection to the east, and intermittent deep-mantle plumes, leaves a remarkable tectonic signature in the MTZ beneath eastern North America.

6. Conclusion

We have performed an extensive analysis of the structure of the mantle transition zone (MTZ) beneath eastern North America, and developed and provided a methodological approach by which to do so. Specifically, we have found that the choice of velocity model used to depth-convert receiver functions can lead to significant variations in the observed depths of the 410 and 660 km discontinuities. The overall MTZ thickness, however, is found to be less sensitive to the differences in velocity models, and is therefore a robust feature when it comes to interpreting receiver function results in their respective geologic and geodynamic contexts. With this in mind, we explored a variety of significant features in our dataset: notably, the Northern Appalachian Anomaly (NAA), the Central Appalachian Anomaly (CAA), and Laramide slab anomaly. These features correspond to positive and negative thermal anomalies on the order of ±100 K, which may seem modest beneath an active margin or mantle plume, but are noteworthy considering the current status of the region as a passive "volcanic" margin. These observations enhance our understanding of the NAA and CAA, suggesting that they may penetrate into the MTZ instead of being solely confined to shallow asthenospheric depths. Our observations of the stagnant Laramide slab provide additional evidence for slabs stalling in the MTZ, and reinforce the theory of two-stage subduction of the Farallon slab.

Supplementary data to this article can be found online at https://doi.org/10.1016/j.pepi.2023.107035.

Declaration of Competing Interest

The authors declare that they have no known competing financial interests or personal relationships that could have appeared to influence the work reported in this paper.

Data availability

All data used in this study are available from the EarthScope Consortium at: http://ds.iris.edu. Code used for this paper can be found at: https://github.com/alexburky.

Acknowledgments

The computer code developed for this work, `rflexa` (Burky et al., 2021a), is available online at: `https://github.com/alexburky/rflexa`. We acknowledge the use of the Seismic Analysis Code (SAC) Version 101.6a (Goldstein and Snoke, 2005). Data for this study were provided by the IRIS DMC (doi: https://doi.org/10.7914/SN/TA). This work was partly supported by the U.S. National Science Foundation (NSF) under grants EAR-1736046 and OCE-1917085, and by Princeton University. High-performance computing resources were provided by the Princeton Institute for Computational Science & Engineering (PICSciE). We would like to thank Vadim Levin and Blair Schoene for helpful feedback on the manuscript, as well as Ana Ferreira and three anonymous reviewers who helped to greatly improve the quality of this study.

References

Agee, J.J., Garrison, J.R., Taylor, L.A., 1982. Petrogenesis of oxide minerals in kimberlite, Elliott County, Kentucky. Am. Mineral. 67, 28–42.

Akaogi, M., Takayama, H., Kojitani, H., Kawaji, H., Atake, T., 2007. Low-temperature heat capacities, entropies and enthalpies of Mg_2SiO_4 polymorphs, and α-β-γ and post-spinel phase relations at high pressure. Phys. Chem. Miner. 34, 169–183. https://doi.org/10.1007/s00269–006–0137–3.

Bassin, C., Laske, G., Masters, G., 2000. The current limits of resolution for surface wave tomography in North America. Eos Trans. AGU 81, F897.

Brunsvik, B.R., Eilon, Z.C., Lynner, C., 2021. Mantle structure and flow across the continent-ocean transition of the eastern North American margin: anisotropic *S*-wave tomography. Geochem. Geophys. Geosyst. 22 https://doi.org/10.1029/2021GC010084 e2021GC010084.

Burky, A.L., Irving, J.C.E., Simons, F.J., 2021a. Instrument response removal and the 2020 M_{Lg} 3.1 Marlboro, New Jersey, earthquake. Seismol. Res. Lett. 92, 3865–3872. https://doi.org/10.1785/0220210118.

Burky, A.L., Irving, J.C.E., Simons, F.J., 2021b. Mantle transition zone receiver functions for Bermuda: automation, quality control, and interpretation. J. Geophys. Res. 126 https://doi.org/10.1029/2020JB020177 e2020JB020177.

Byrnes, J.S., Bezada, M., Long, M.D., Benoit, M.H., 2019. Thin lithosphere beneath the central Appalachian Mountains: constraints from seismic attenuation beneath the MAGIC array. Earth Planet. Sci. Lett. 519, 297–307. https://doi.org/10.1016/j.epsl.2019.04.045.

Chang, S.-J., Ferreira, A.M.G., Ritsema, J., van Heijst, H.J., Woodhouse, J.H., 2014. Global radially anisotropic mantle structure from multiple datasets: a review, current challenges, and outlook. Tectonophysics 617, 1–19. https://doi.org/10.1016/j.tecto.2014.01.033.

Chang, S.-J., Ferreira, A.M.G., Ritsema, J., van Heijst, H.J., Woodhouse, J.H., 2015. Joint inversion for global isotropic and radially anisotropic mantle structure including crustal thickness perturbations. J. Geophys. Res. 120, 4278–4300. https://doi.org/10.1002/2014JB011824.

Chevrot, S., Vinnik, L., Montagner, J.-P., 1999. Global scale analysis of mantle *Pds* phases. J. Geophys. Res. 104, 20203–20219. https://doi.org/10.1029/1999JB900087.

Chu, R., Leng, W., Helmberger, D.V., Gurnis, M., 2013. Hidden hotspot track beneath the eastern United States. Nat. Geosci. 6, 963–966. https://doi.org/10.1038/ngeo1949.

Crotwell, H.P., Owens, T.J., Ritsema, J., 1999. The TauP toolkit: flexible seismic travel-time and ray-path utilities. Seismol. Res. Lett. 70, 154–160. https://doi.org/10.1785/gssrl.70.2.154.

Deuss, A., Andrews, J., Day, E., 2013. Seismic observations of mantle discontinuities and their mineralogical and dynamical interpretation. In: Karato, S.-I. (Ed.), Physics and

Chemistry of the Deep Earth Chapter 10. John Wiley, New York, pp. 295–323. https://doi.org/10.1002/9781118529492.ch10).
Dueker, K.G., Sheehan, A.F., 1997. Mantle discontinuity structure from midpoint stacks of converted *P* to *S* waves across the Yellowstone hotspot track. J. Geophys. Res. 102, 8313–8327. https://doi.org/10.1029/96JB03857.
Gao, S.S., Liu, K.H., 2014. Mantle transition zone discontinuities beneath the contiguous United States. J. Geophys. Res. 119, 6452–6468. https://doi.org/10.1002/2014JB011253.
Geoffroy, L., 2005. Volcanic passive margins. Compt. Rendus Geosci. 337, 1395–1408. https://doi.org/10.1016/j.crte.2005.10.006.
Goldstein, P., Snoke, A., 2005. SAC Availability for the IRIS Community, 7. Incorporated Research Institutions for Seismology Newsletter.
Golos, E.M., Fang, H., Yao, H., Zhang, H., Burdick, S., Vernon, F., Schaeffer, A., Lebedev, S., van der Hilst, R.D., 2018. Shear wave tomography beneath the United States using a joint inversion of surface and body waves. J. Geophys. Res. 123, 5169–5189. https://doi.org/10.1029/2017JB014894.
Hatcher, R.D., Tollo, R.P., Bartholomew, M.J., Hibbard, J.P., Karabinos, P.M., 2010. The Appalachian orogen: A brief summary. In: From Rodinia to Pangea: The Lithotectonic Record of the Appalachian Region: Geological Society of America Memoir, 206, pp. 1–19. https://doi.org/10.1130/2010.1206(01).
Helffrich, G.R., 2000. Topography of the transition zone seismic discontinuities. Rev. Geophys. 38, 141–158. https://doi.org/10.1029/1999RG000060.
Houser, C., 2016. Global seismic data reveal little water in the mantle transition zone. Earth Planet. Sci. Lett. 448, 94–101. https://doi.org/10.1016/j.epsl.2016.04.018.
Huang, Q., Schmerr, N., Waszek, L., Beghein, C., 2019. Constraints on seismic anisotropy in the mantle transition zone from long-period *SS* precursors. J. Geophys. Res. 124, 6779–6800. https://doi.org/10.1029/2019JB017307.
Humphreys, E.D., Schmandt, B., Bezada, M.J., Perry-Houts, J., 2015. Recent craton growth by slab stacking beneath Wyoming. Earth Planet. Sci. Lett. 429, 170–180. https://doi.org/10.1016/j.epsl.2015.07.066.
Jackson, M.G., Konter, J.G., Becker, T.W., 2017. Primordial helium entrained by the hottest mantle plumes. Nature 542, 340–343. https://doi.org/10.1038/nature21023.
Keifer, I., Dueker, K., 2019. Testing the hypothesis that temperature modulates 410 and 660 discontinuity topography beneath the eastern United States. Earth Planet. Sci. Lett. 524, 115723 https://doi.org/10.1016/j.epsl.2019.115723.
Kennett, B.L.N., Engdahl, E.R., 1991. Traveltimes for global earthquake location and phase identification. Geophys. J. Int. 105, 429–465. https://doi.org/10.1111/j.1365–246X.1991.tb06724.x.
Kennett, B.L.N., Engdahl, E.R., Buland, R., 1995. Constraints on seismic velocities in the Earth from traveltimes. Geophys. J. Int. 122, 108–124. https://doi.org/10.1111/j.1365–246X.1995.tb03540.x.
King, S.D., Anderson, D.L., 1998. Edge-driven convection. Earth Planet. Sci. Lett. 160, 289–296. https://doi.org/10.1016/S0012–821X(98)00089–2.
Kinney, S.T., MacLennan, S.A., Keller, C.B., Schoene, B., Setera, J.B., VanTongeren, J.A., Olsen, P.E., 2021. Zircon U-Pb geochronology constrains continental expression of Great Meteor Hotspot magmatism. Geophys. Res. Lett. 48 https://doi.org/10.1029/2020GL091390 e2020GL091390.
Kojitani, H., Inoue, T., Akaogi, M., 2016. Precise measurements of enthalpy of postspinel transition in Mg_2SiO_4 and application to the phase boundary calculation. J. Geophys. Res. 121, 729–742. https://doi.org/10.1002/2015JB012211.
Laske, G., Masters, G., Ma, Z., Pasyanos, M., 2013. Update on CRUST1.0 — A 1-degree global model of Earth's crust. Geophys. Res. Abstr. 15. EGU2013–2658.
Lawrence, J.F., Shearer, P.M., 2006. A global study of transition zone thickness using receiver functions. J. Geophys. Res. 111, B06307. https://doi.org/10.1029/2005JB003973.
Lei, W., Ruan, Y., Bozdag, E., Peter, D., Lefebvre, M., Komatitsch, D., Tromp, J., Hill, J., Podhorszki, N., Pugmire, D., 2020. Global adjoint tomography–model GLAD-M25. Geophys. J. Int. 223, 1–21. https://doi.org/10.1093/gji/ggaa253.
Levin, V., Menke, W., Park, J., 2000. No regional anisotropic domains in the northeastern US Appalachians. J. Geophys. Res. 105, 19029–19042. https://doi.org/10.1029/2000JB900123.
Levin, V., Long, M.D., Skryzalin, P., Li, Y., López, I., 2018. Seismic evidence for a recently formed mantle upwelling beneath New England. Geology 46, 87–90. https://doi.org/10.1130/G39641.1.
Li, A., Fischer, K.M., Wysession, M.E., Clarke, T.J., 1998. Mantle discontinuities and temperature under the North American continental keel. Nature 395, 160–163. https://doi.org/10.1038/25972.
Ligorra, J.P., Ammon, C.J., 1999. Iterative deconvolution and receiver-function estimation. B. Seismol. Soc. Am. 89, 1395–1400. https://doi.org/10.1785/BSSA0890051395.
Long, M.D., Benoit, M.H., Chapman, M.C., King, S.D., 2010. Upper mantle anisotropy and transition zone thickness beneath southeastern North America and implications for mantle dynamics. Geochem. Geophys. Geosyst. 11 https://doi.org/10.1029/2010GC003247.
Long, M.D., Levander, A., Shearer, P.M., 2014. An introduction to the special issue of Earth and Planetary Science Letters on USArray science. Earth Planet. Sci. Lett. 402, 1–5. https://doi.org/10.1016/j.epsl.2014.06.016.
Long, M.D., Jackson, K.G., McNamara, J.F., 2016. *SKS* splitting beneath transportable array stations in eastern North America and the signature of past lithospheric deformation. Geochem. Geophys. Geosyst. 17, 2–15. https://doi.org/10.1002/2015GC006088.
Maguire, R., Ritsema, J., Goes, S., 2018. Evidence of subduction-related thermal and compositional heterogeneity below the United States from transition zone receiver functions. Geophys. Res. Lett. 45, 8913–8922. https://doi.org/10.1029/2018GL078378.
Mao, W., Gurnis, M., Wu, W., 2022. On the origin of small-scale seismic scatters at 660-km depth. Geochem. Geophys. Geosyst. 23 https://doi.org/10.1029/2022GC010560 e2022GC010560.
Mazza, S.E., Gazel, E., Johnson, E.A., Kunk, M.J., McAleer, R., A, J.S., Bizimis, M., Coleman, D.S., 2014. Volcanoes of the passive margin: the youngest magmatic event in eastern North America. Geology 42, 483–486. https://doi.org/10.1130/G35407.1.
Mazza, S.E., Gazel, E., Bizimis, M., Moucha, R., Béguelin, P., Johnson, E.A., McAleer, R. J., Sobolev, A.V., 2019. Sampling the volatile-rich transition zone beneath Bermuda. Nature 569, 398–403. https://doi.org/10.1038/s41586–019–1183–6.
Menke, W., Skryzalin, P., Levin, V., Harper, T., Darbyshire, F., Dong, T., 2016. The northern Appalachian anomaly: a modern asthenospheric upwelling. Geophys. Res. Lett. 43, 10–173. https://doi.org/10.1002/2016GL070918.
Morgan, W.J., 1971. Convection plumes in the lower mantle. Nature 230, 42–43. https://doi.org/10.1038/230042a0.
Muir, J.M.R., Zhang, F., Brodholt, J.P., 2021. The effect of water on the post-spinel transition and evidence for extreme water contents at the bottom of the transition zone. Earth Planet. Sci. Lett. 565, 116909 https://doi.org/10.1016/j.epsl.2021.116909.
Nelson, K.D., 1992. Are crustal thickness variations in old mountain belts like the Appalachians a consequence of lithospheric delamination? Geology 20, 498–502. https://doi.org/10.1130/0091–7613(1992)020<0498:ACTVIO>.3.CO;2.
Page, M.T., Hough, S.E., 2014. The New Madrid seismic zone: not dead yet. Science 343, 762–764. https://doi.org/10.1126/science.1248215.
Savage, B., 2021. Body wave speed structure of eastern North America. Geochem. Geophys. Geosyst. 22 https://doi.org/10.1029/2020GC009002 e2020GC009002.
Schaeffer, A.J., Lebedev, S., 2014. Imaging the North American continent using waveform inversion of global and USArray data. Earth Planet. Sci. Lett. 402, 26–41. https://doi.org/10.1016/j.epsl.2014.05.014.
Schmandt, B., Lin, F.-C., 2014. *P* and *S* wave tomography of the mantle beneath the United States. Geophys. Res. Lett. 41, 6342–6349. https://doi.org/10.1002/2014GL061231.
Shearer, P.M., Buehler, J., 2019. Imaging upper-mantle structure under USArray using long-period reflection seismology. J. Geophys. Res. 124, 9638–9652. https://doi.org/10.1029/2019JB017326.
Sigloch, K., 2011. Mantle provinces under North America from multifrequency *P* wave tomography. Geochem. Geophys. Geosyst. 12 https://doi.org/10.1029/2010GC003421.
Sigloch, K., McQuarrie, N., Nolet, G., 2008. Two-stage subduction history under North America inferred from multiple-frequency tomography. Nat. Geosci. 1, 458–462. https://doi.org/10.1038/ngeo231.
Simmons, N.A., Forte, A.M., Boschi, L., Grand, S.P., 2010. GyPSuM: a joint tomographic model of mantle density and seismic wave speeds. J. Geophys. Res. 115, B12310. https://doi.org/10.1029/2010JB007631.
Simmons, N.A., Myers, S.C., Johannesson, G., Matzel, E., 2012. LLNL-G3Dv3: global *P* wave tomography model for improved regional and teleseismic travel time prediction. J. Geophys. Res. 117, B10302. https://doi.org/10.1029/2012JB009525.
Simmons, N.A., Myers, S.C., Morency, C., Chiang, A., Knapp, D.R., 2021. SPiRaL: a multiresolution global tomography model of seismic wave speeds and radial anisotropy variations in the crust and mantle. Geophys. J. Int. 227, 1366–1391. https://doi.org/10.1093/gji/ggab277.
Sleep, N.H., 1990. Hotspots and mantle plumes: some phenomenology. J. Geophys. Res. 95, 6715–6736. https://doi.org/10.1029/JB095iB05p06715.
Torgersen, T., Drenkard, S., Stute, M., Schlosser, P., Shapiro, A., 1995. Mantle helium in ground waters of eastern North America: time and space constraints on sources. Geology 23, 675–678. https://doi.org/10.1130/0091–7613(1995)023<0675:MHIGWO>2.3.CO;2.
van der Lee, S., Regenauer-Lieb, K., Yuen, D.A., 2008. The role of water in connecting past and future episodes of subduction. Earth Planet. Sci. Lett. 273, 15–27. https://doi.org/10.1016/j.epsl.2008.04.041.
van Stiphout, A.M., Cottaar, S., Deuss, A., 2019. Receiver function mapping of mantle transition zone discontinuities beneath Alaska using scaled 3-D velocity corrections. Geophys. J. Int. 219, 1432–1446. https://doi.org/10.1093/gji/ggz360.
Vogt, P., Jung, W.-Y., 2007. Origin of the Bermuda volcanoes and the Bermuda Rise: history, observations, models, and puzzles. Geol. Soc. Am. Spec. Pap. 430, 553–591. https://doi.org/10.1130/SPE430.
Wang, H., Zhao, D., Huang, Z., Wang, L., 2019. Tomography, seismotectonics, and mantle dynamics of central and eastern United States. J. Geophys. Res. 124, 8890–8907. https://doi.org/10.1029/2019JB017478.
Wu, W., Ni, S., Irving, J.C.E., 2019. Inferring Earth's discontinuous chemical layering from the 660-kilometer boundary topography. Science 363, 736–740. https://doi.org/10.1126/science.aav0822.
Yu, Y.G., Wu, Z., Wentzcovitch, R.M., 2008. α–β–γ transformations in Mg_2SiO_4 in Earth′s transition zone. Earth Planet. Sci. Lett. 273, 115–122. https://doi.org/10.1016/j.epsl.2008.06.023.
Zhang, H., Schmandt, B., Zhou, W.-Y., Zhang, J.S., Maguire, R., 2022. A single 520 km discontinuity beneath the contiguous United States with pyrolitic seismic properties. Geophys. Res. Lett. 49 https://doi.org/10.1029/2022GL101300 e2022GL101300.
Zhang, Z., Irving, J.C.E., Simons, F.J., Alkhalifah, T., 2023. Seismic evidence for a 1000 km mantle discontinuity under the Pacific. Nat. Commun. 14 (1), 1714. https://doi.org/10.1038/s41467-023-37067-x.

SUPPLEMENTARY MATERIAL

The mantle transition zone beneath eastern North America: Receiver functions and tomographic velocity models

Alexander L. Burky, Jessica C. E. Irving, and Frederik J. Simons

This document contains 21 Figures and 1 Table as a supplement to the Main Text. Each of the figures is referenced in the Main Text, and a thorough description of each figure is provided in the captions. The video animations mentioned in the Main Text can be found on the site where this Supplement was accessed.

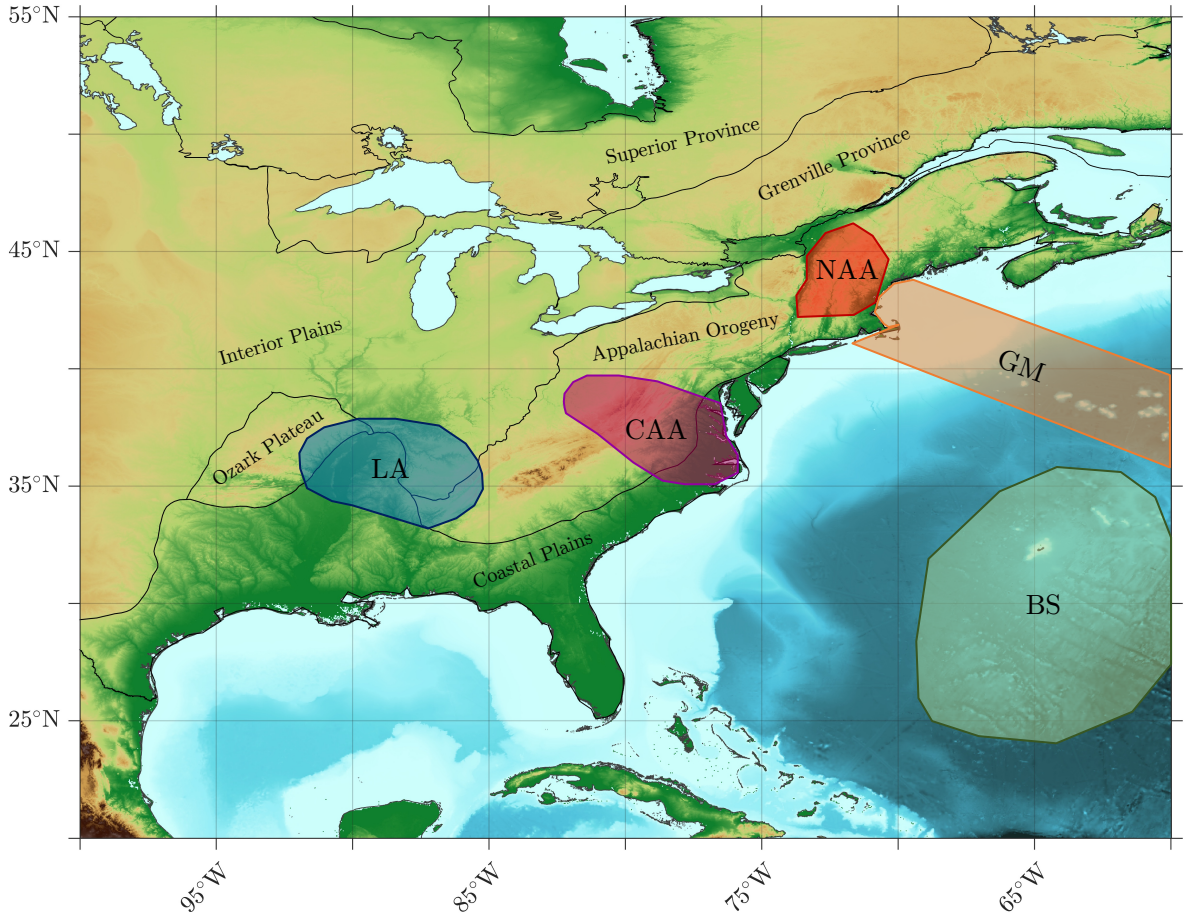

Figure S1: Summary map showing the tectonic provinces of eastern North America and the western Atlantic, overlain with markers indicating the MTZ features mentioned in the Main Text. The labels represent, BS: Bermuda Swell, CAA: Central Appalachian Anomaly, GM: Great Meteor hotspot track, LA: Laramide slab Anomaly, and NAA: Northern Appalachian Anomaly, respectively. The connection between the offshore magmatic events and the Appalachian anomalies remains uncertain, and could be better understood with offshore seismic deployments in the region.

North American Mantle Transition Zone Thickness Observations				
3-D model	GLADM25	GyPSuM	LLNL_G3D_JPS	SL2013NA
$\bar{z} + 2\sigma$	259 km	253 km	256 km	252 km
$\bar{z}$	**246 km**	**241 km**	**242 km**	**241 km**
$\bar{z} - 2\sigma$	233 km	229 km	228 km	230 km
Northern Appalachian Anomaly				
$\bar{z} + 2\sigma$	245 km	244 km	244 km	243 km
$\bar{z}$	**238 km**	**236 km**	**235 km**	**238 km**
$\bar{z} - 2\sigma$	231 km	228 km	227 km	232 km
z_{min}	229 km	224 km	223 km	227 km
Central Appalachian Anomaly				
$\bar{z} + 2\sigma$	244 km	244 km	245 km	243 km
$\bar{z}$	**238 km**	**236 km**	**236 km**	**237 km**
$\bar{z} - 2\sigma$	233 km	228 km	227 km	231 km
z_{min}	228 km	216 km	214 km	228 km
Laramide Slab Anomaly				
z_{max}	263 km	257 km	262 km	257 km
$\bar{z} + 2\sigma$	257 km	251 km	256 km	251 km
$\bar{z}$	**249 km**	**246 km**	**248 km**	**245 km**
$\bar{z} - 2\sigma$	240 km	240 km	240 km	240 km

Table S1: Mantle transition zone (MTZ) thickness observations from our study. The top of the table summarizes the entire dataset, and the three sections underneath summarize measurements of the Northern Appalachian Anomaly (NAA), Central Appalachian Anomaly (CAA), and Laramide Slab Anomaly. For the NAA and CAA, statistics are reported ($\bar{z}$ is the mean MTZ thickness, σ the standard deviation, and z_{min} and z_{max} the minima and maxima) for below the 242 km contour line in the enclosed regions shown in Figs S2 and S3. Areas above the 242 km contour line for the region enclosed shown in Fig. S4 are used for the Laramide Slab Anomaly. Note that the minima and maxima associated with all three anomalies are outside of the 2σ range.

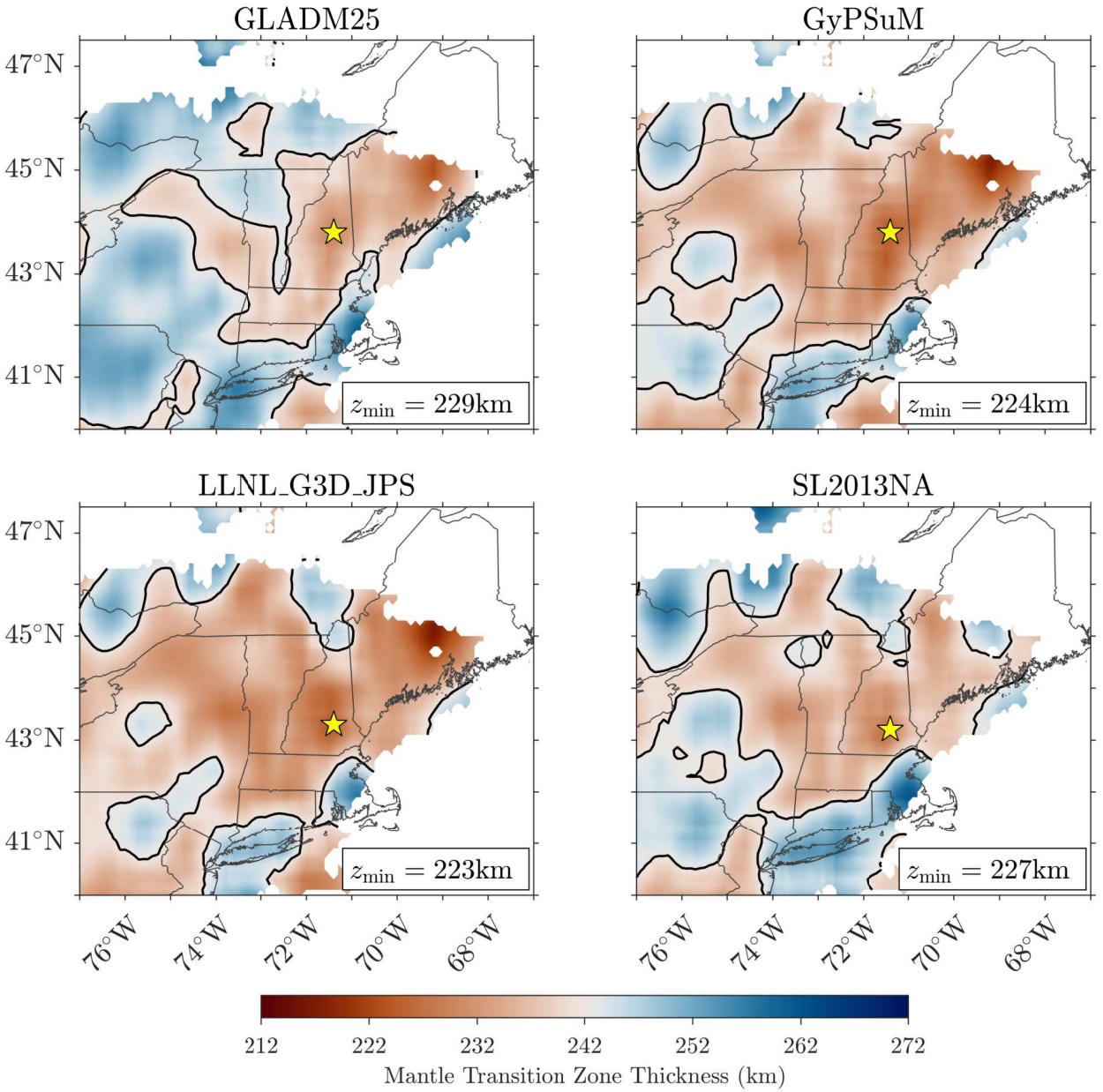

Figure S2: Maps showing the measured MTZ thickness in the region containing the Northern Appalachian Anomaly (NAA), for the four different 3-D models identified in the titles. The stars indicate the locations of the minimum thickness, z_{min}, used in the Main Text to estimate the upper limit on the magnitude of the warm thermal anomaly. We have restricted this measurement to be reasonably far from the edges of this region where data coverage is less robust. The solid black contour lines denote the 242 km level, which corresponds to the global average (Lawrence & Shearer, 2006).

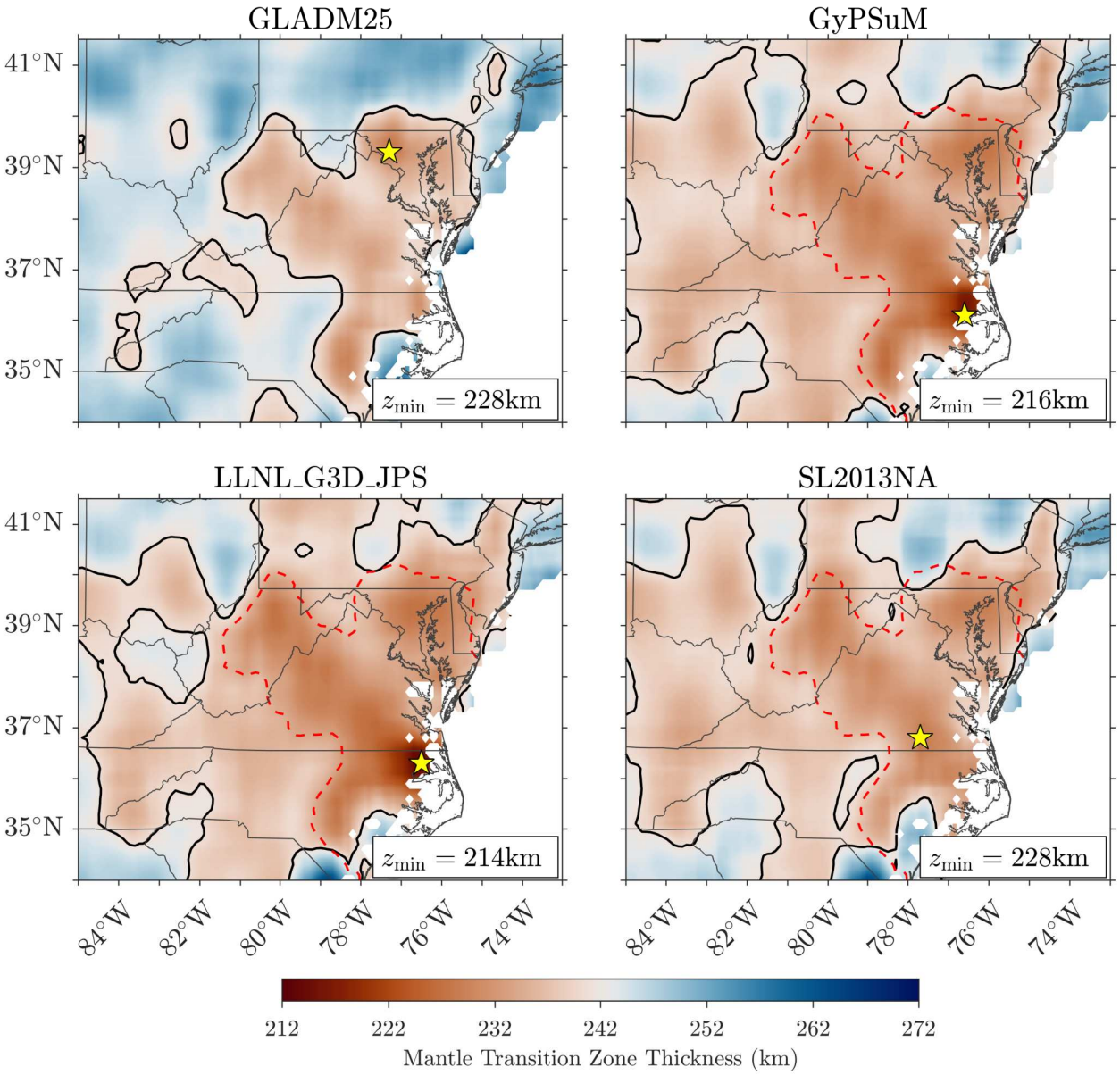

Figure S3: Maps showing the measured MTZ thickness in the region containing the Central Appalachian Anomaly (CAA). Same layout as Fig. S2, however, the black contour line is drawn at 241 km to better highlight the feature in model GLADM25. Note that the thinning is more pronounced when depth-converting with models GyPSuM and LLNL_G3D_JPS, consistent with Fig. S2. The extent of the anomaly is consistent beneath Maryland, Virginia, and eastern West Virginia across all four models. This can be seen from the contour extracted from model GLADM25 (dashed red lines) overlain on the other three models.

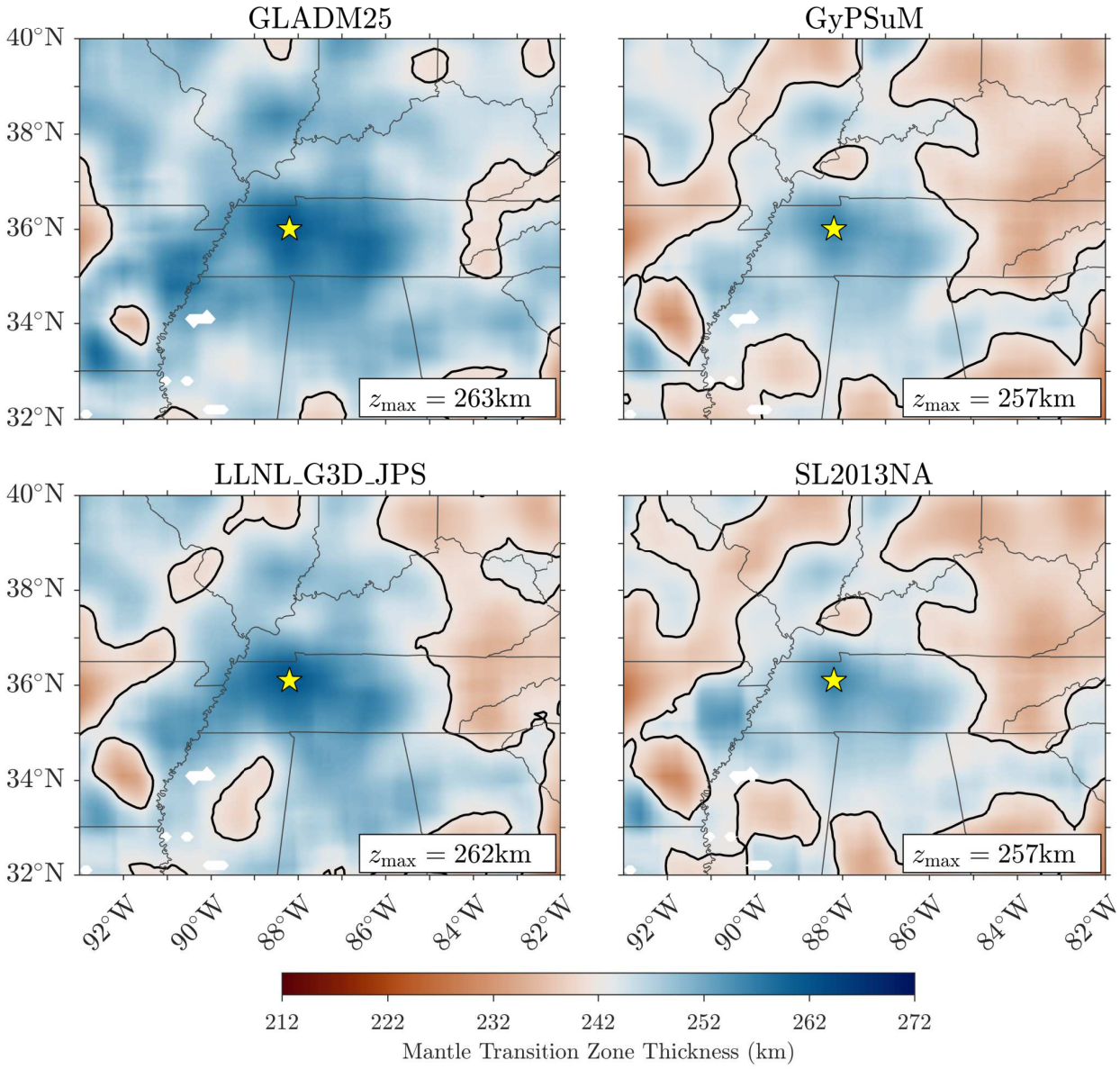

Figure S4: Maps showing the measured MTZ thickness in the region containing the the thickened MTZ anomaly beneath western Tennessee. Same layout as Fig. S2, however, the stars now indicate the locations of the maximum thickness, z_{max}, used in the Main Text to estimate the upper limit on the magnitude of the cold thermal anomaly. Note that the location of the maximum thickness is consistent across all four models, and that the geometry of the anomaly is also roughly consistent. The range of the maximum thickness anomaly (6 km variation) is fairly small between all four models.

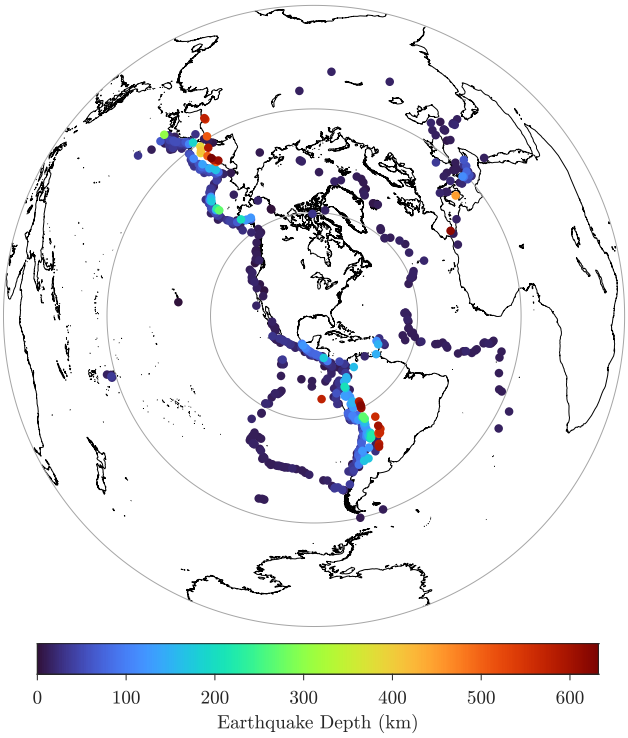

Figure S5: Depths of the earthquakes which contributed to the accepted receiver functions used in our study. Note the increasing depths of earthquakes in subduction zones, as expected, and the shallow depths of earthquakes at mid-ocean ridges.

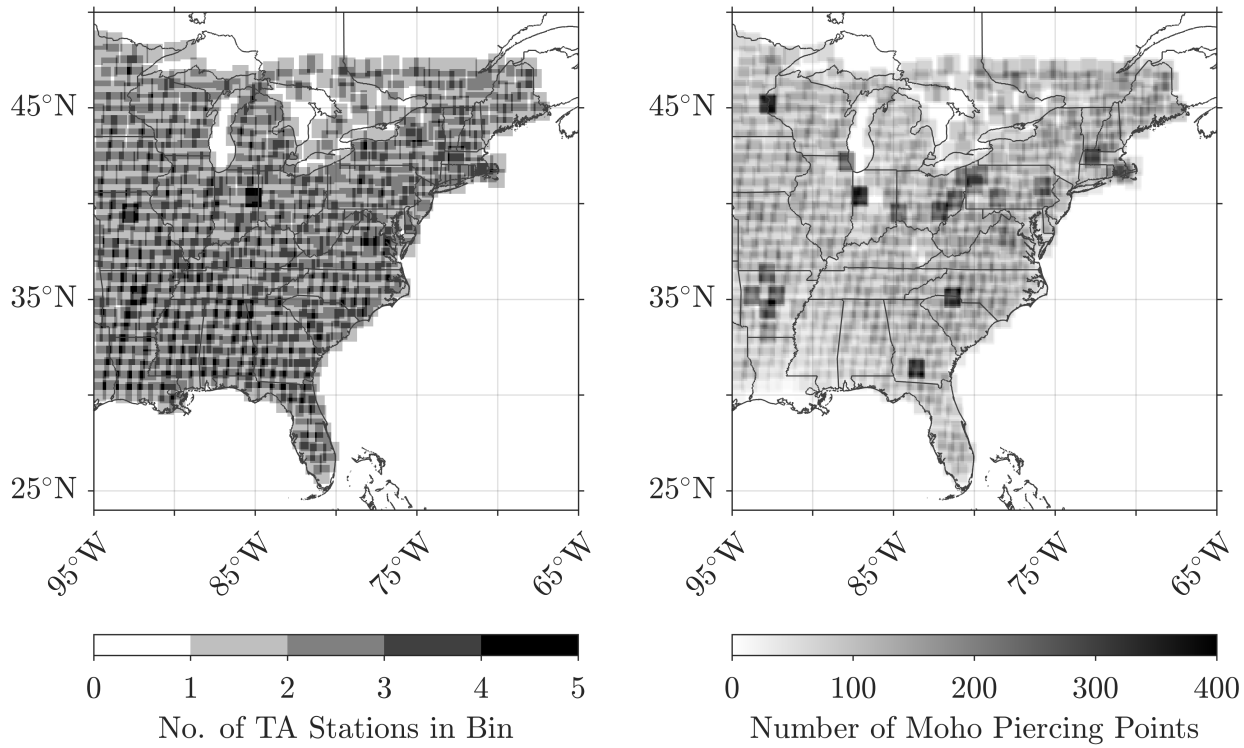

Figure S6: Density maps showing the number of TA stations in each CCP bin (*left*) next to the number of Moho piercing points in each bin (*right*). Certain bins with many stations, combined with exceptional data quality at some stations, lead to the handful of bins with anomalously high numbers of piercing points seen in the figure on the right.

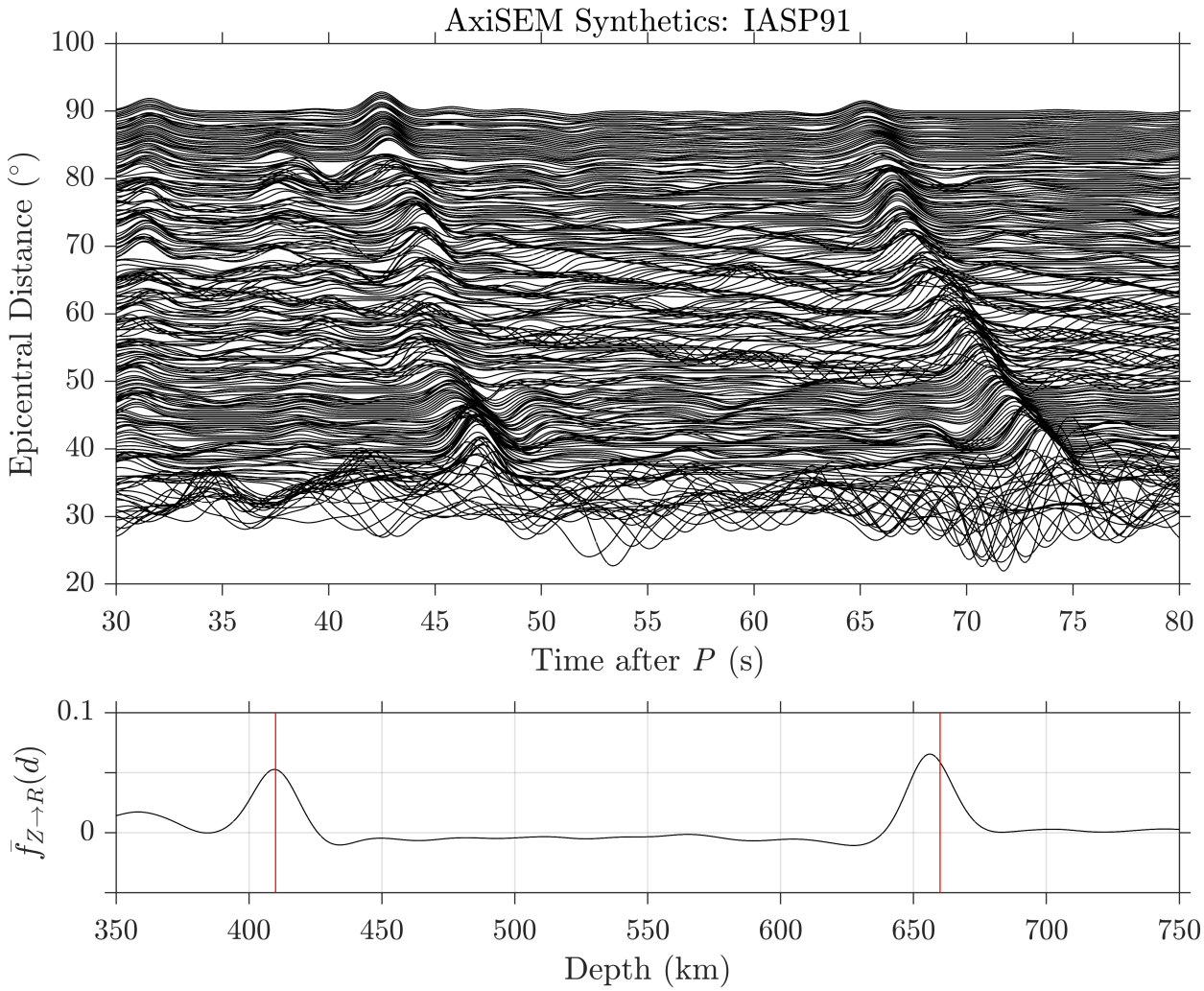

Figure S7: Validation of our methodology for synthetic receiver functions computed from AxiSEM synthetic seismograms (Nissen-Meyer et al., 2014). Synthetics are calculated for model *iasp91* using a 1 Hz dominant period, and are processed using the methodology outlined in the Main Text. Our method is able to successfully resolve the *P410s* and *P660s* phases, with a slight underestimation of the depth of the 660.

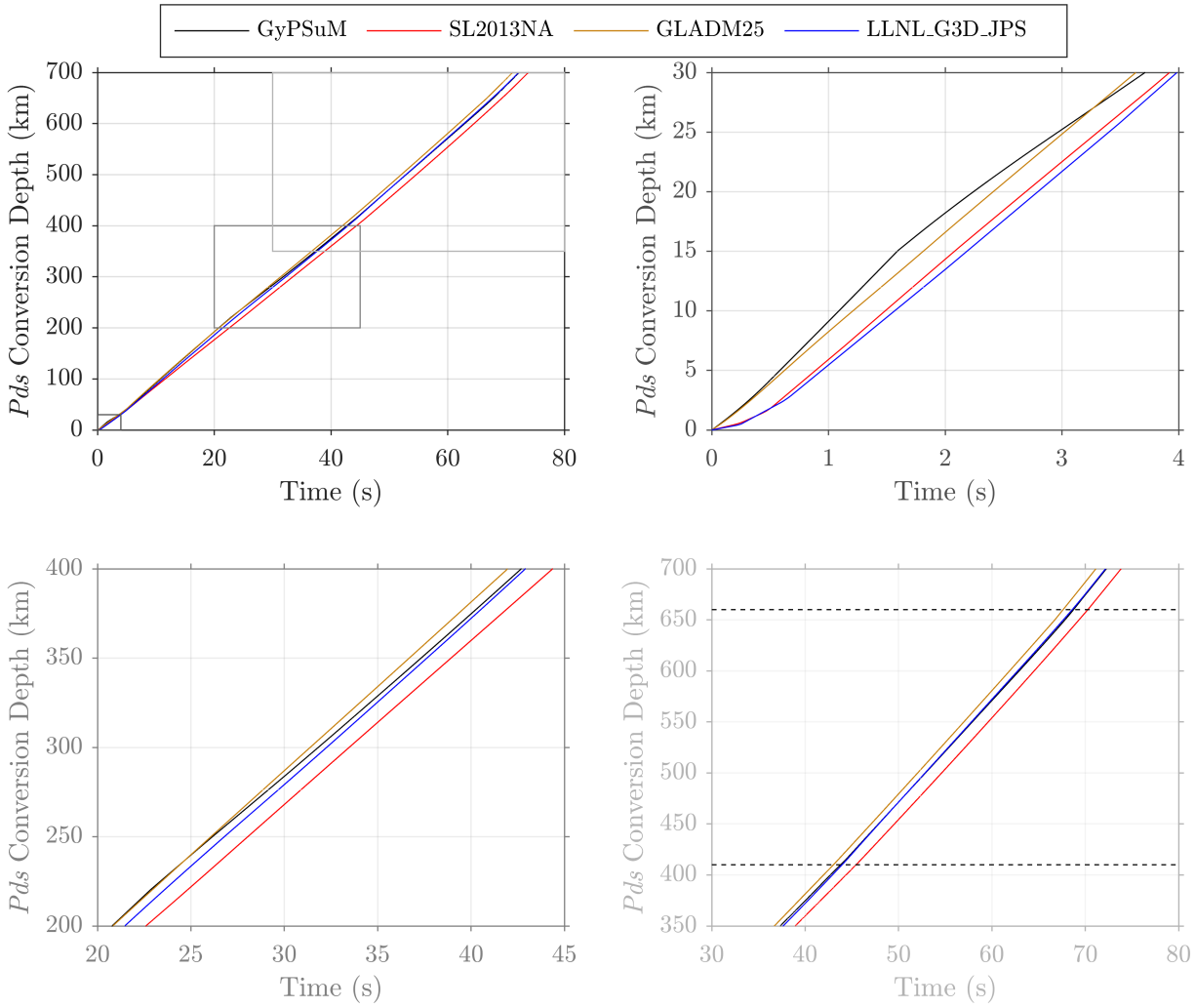

Figure S8: The average relationship between *Pds* conversion depth and time relative to the main *P* arrival for all receiver functions recorded by station TA W41A. These relationships are shown for the four different 3-D velocity models used in our study. They are used to transform receiver functions from the time-domain to the depth-domain. To illustrate how to comprehend these plots, the reader's attention is drawn to the top-right panel. A peak 1 s after the main *P* arrival would be mapped to a depth of ∼5 km using models LLNL_G3D_JPS and SL2013NA, but would be mapped to a depth of ∼9 km with models GLADM25 and GyPSuM. The behavior of these curves in the lower-right panel explains the spread in the 410 and 660 depths seen in Fig. 7 of the Main Text. Since these curves are essentially parallel through the MTZ, the measured MTZ thickness is consistent regardless of the chosen model.

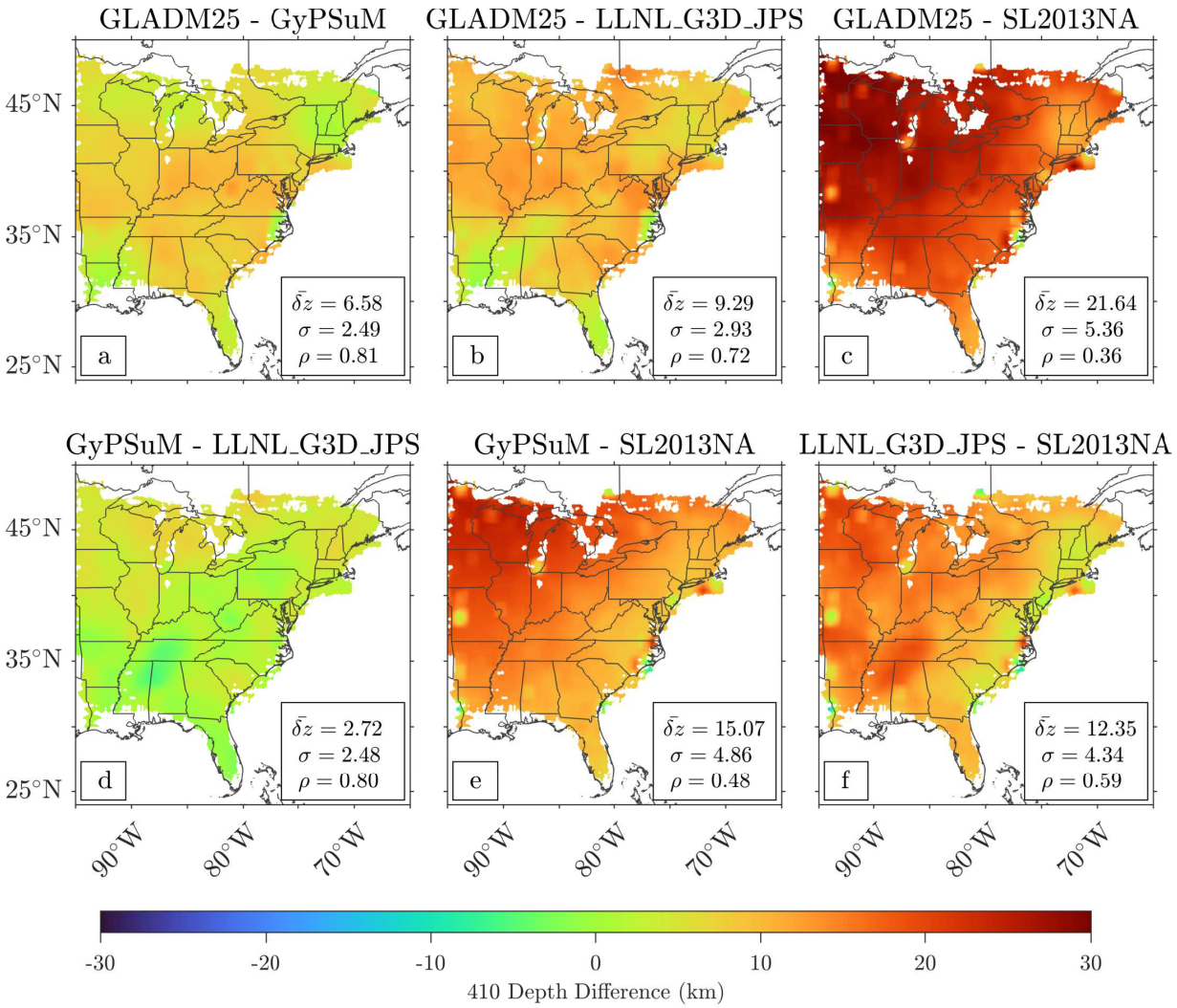

Figure S9: Maps showing the differences in the 410 between each pair of 3-D models, laid out as Fig. 8 of the Main Text. Note that the average differences ($\overline{\delta z}$) between models are greater than they were for the MTZ thickness. The correlation coefficients (ρ) are consistently smaller than for the MTZ thickness, reinforcing the idea that the MTZ thickness is a more robust measurement than the absolute depth of the 410.

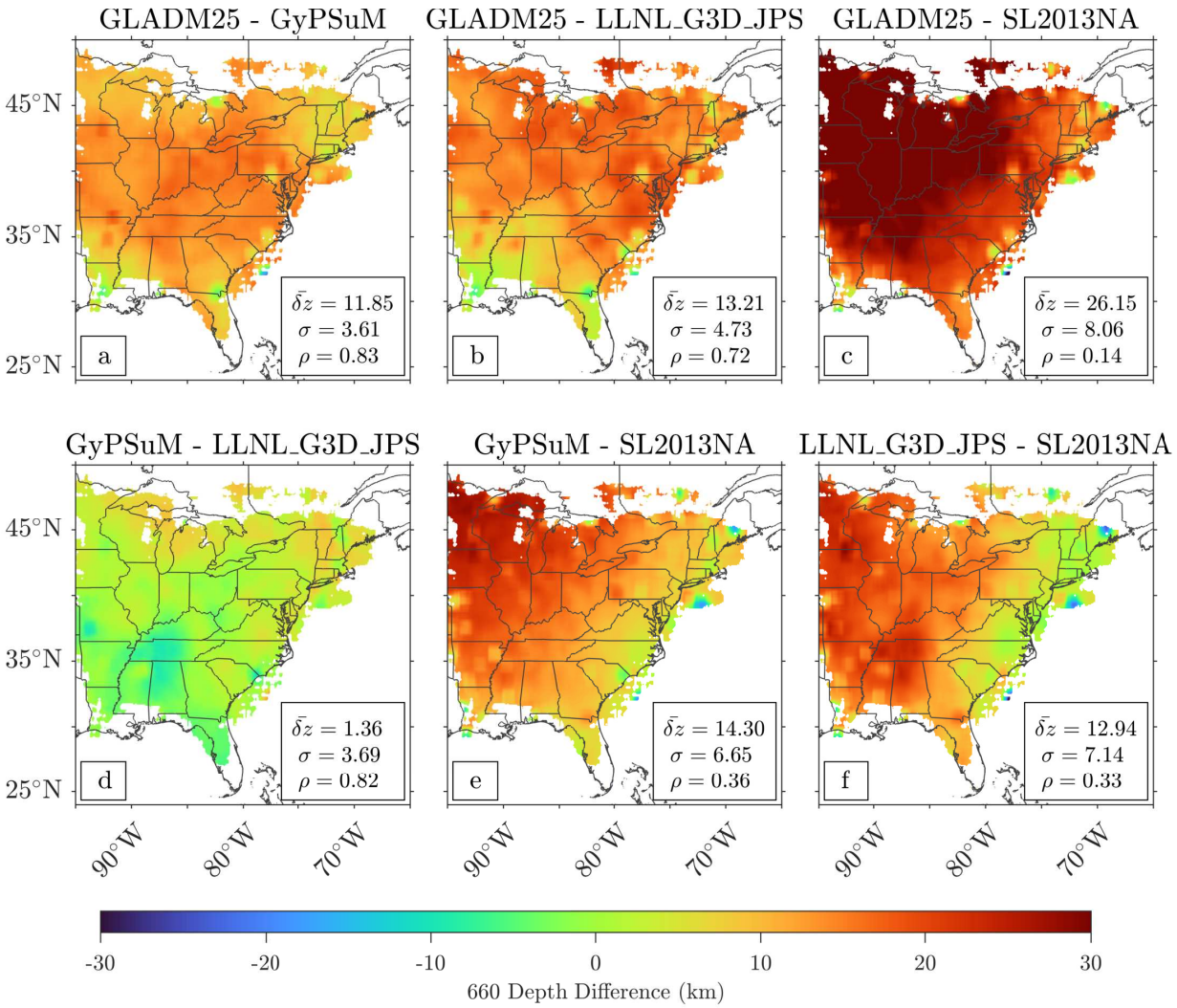

Figure S10: Maps showing the differences in the 660 between each pair of 3-D models, laid out as Fig. S9. Once again note the smaller correlation coefficient between models compared to that of the MTZ thickness shown in Fig. 8 of the Main Text, showing that the MTZ thickness is more robust than the absolute depth of the 660. Model SL2013NA, in particular, shows very poor correlation with the other three models.

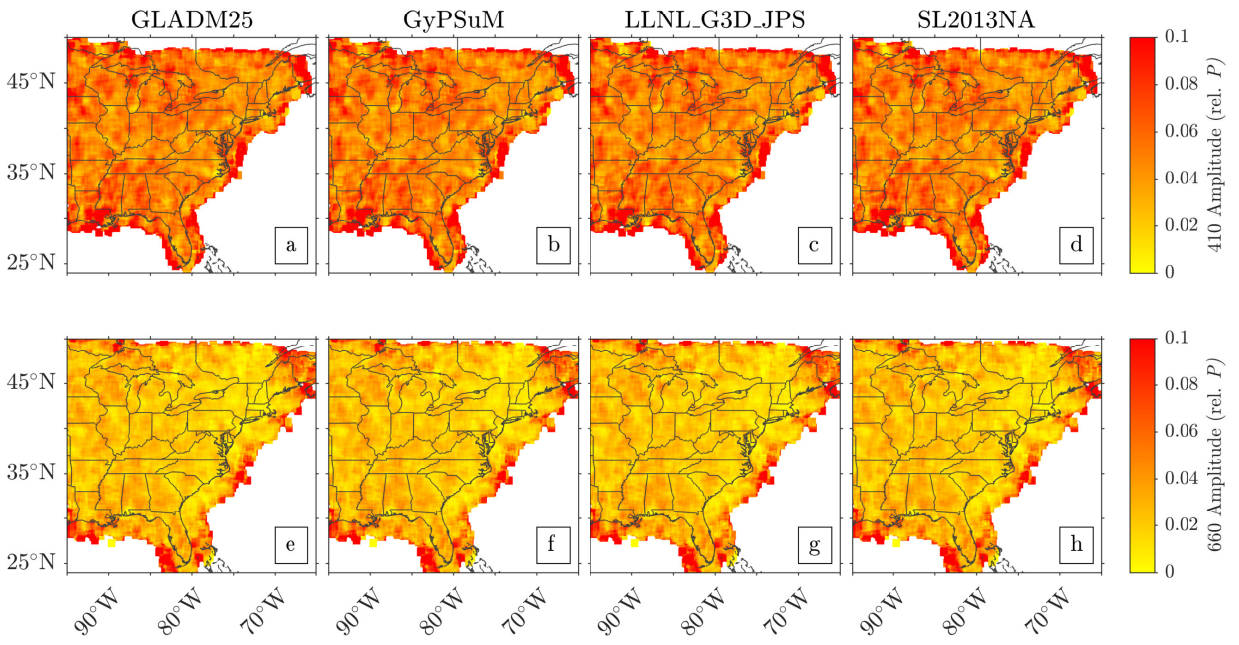

Figure S11: Maps showing the average measured amplitude of the 410 and 660 signals relative to the main P arrival (defined as 1). Note that the 410 signal is consistently larger than the signal from the 660. This can also be seen in the cross sections shown in Figs 4–6 of the Main Text.

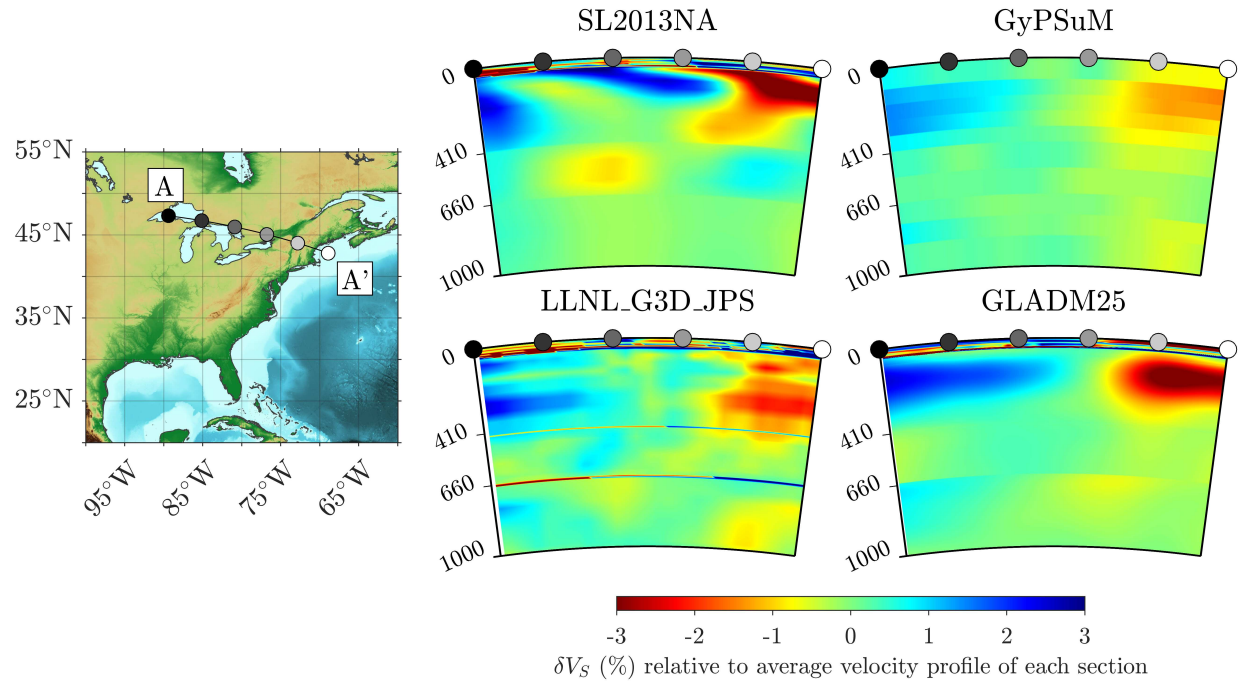

Figure S12: Cross sections along line A-A through the four selected tomography models identified by the titles. Note the presence of a strong low-velocity anomaly beneath New England (the Northern Appalachian Anomaly, NAA). The NAA appears to be confined to the upper mantle above the MTZ, but the receiver function data suggest that it has an effect on the MTZ. Plotted is the percent variation of the S wave velocity from the average one-dimensional velocity profile over the entire cross section.

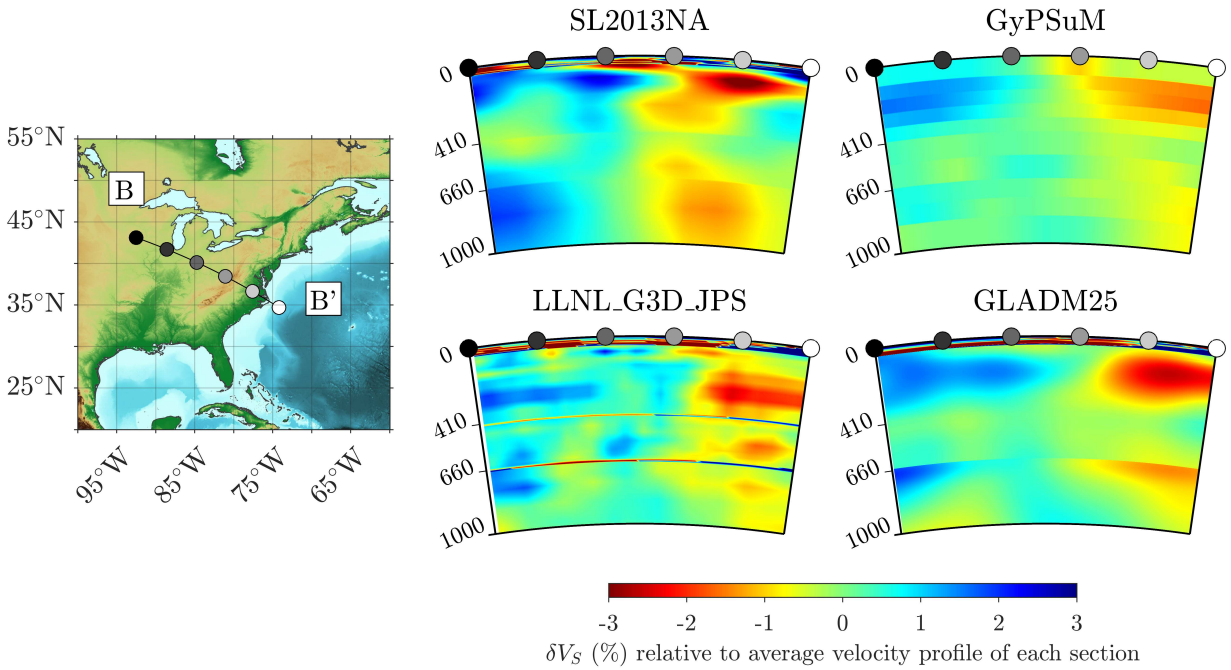

Figure S13: Same as Fig. S12 but for cross section B-B'.

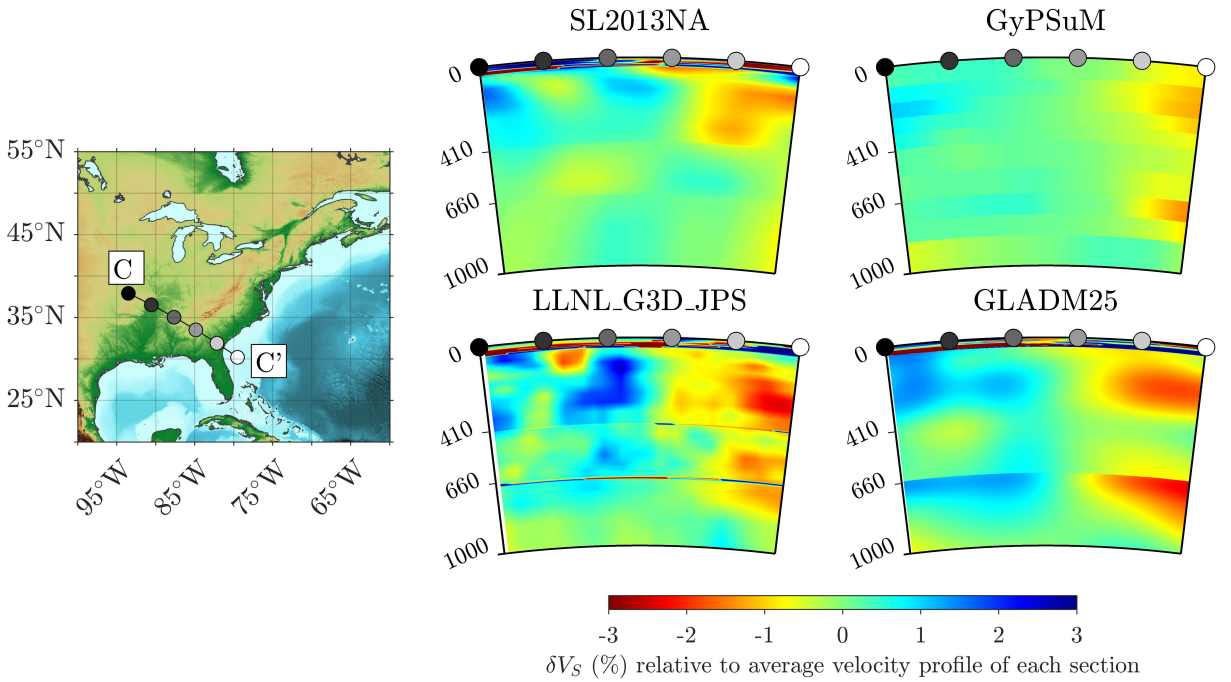

Figure S14: Same as Fig. S12 but for cross section C-C'.

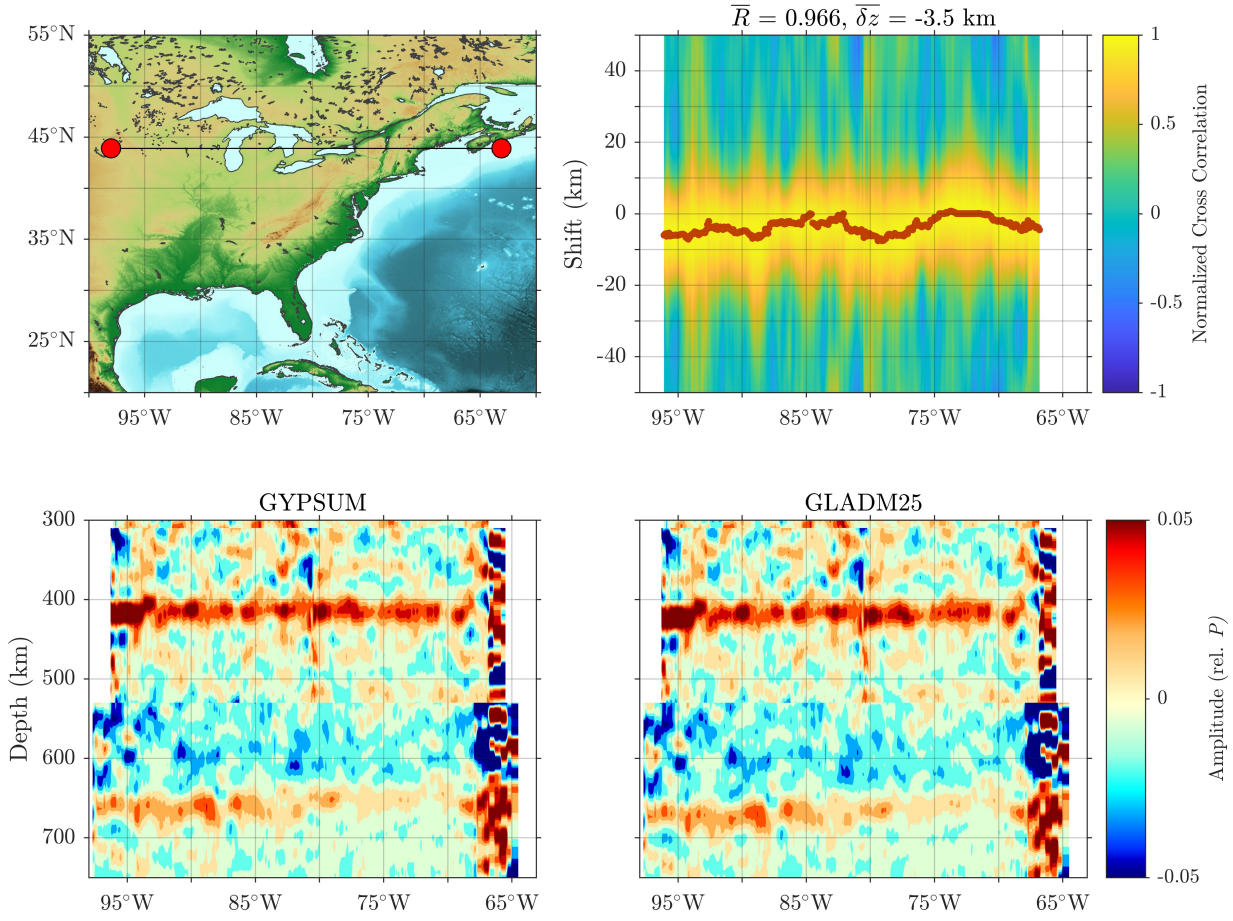

Figure S15: Snapshot from the supplemental videos showing the cross correlation between two CCP stacks. The bottom panel shows the CCP stacks, and the top right panel shows the cross correlation of the two stacks. The red line indicates the maximum of the cross correlation at each longitude. $\bar{R}$ is the average value of the correlation coefficient, and $\bar{\delta z}$ is the average value of the shifts indicated by the red dots. For all of the different CCP stacks, the correlation coefficient tends to be high, but there is a great deal of variability in the relative shifts of the stacks $\bar{\delta z}$.

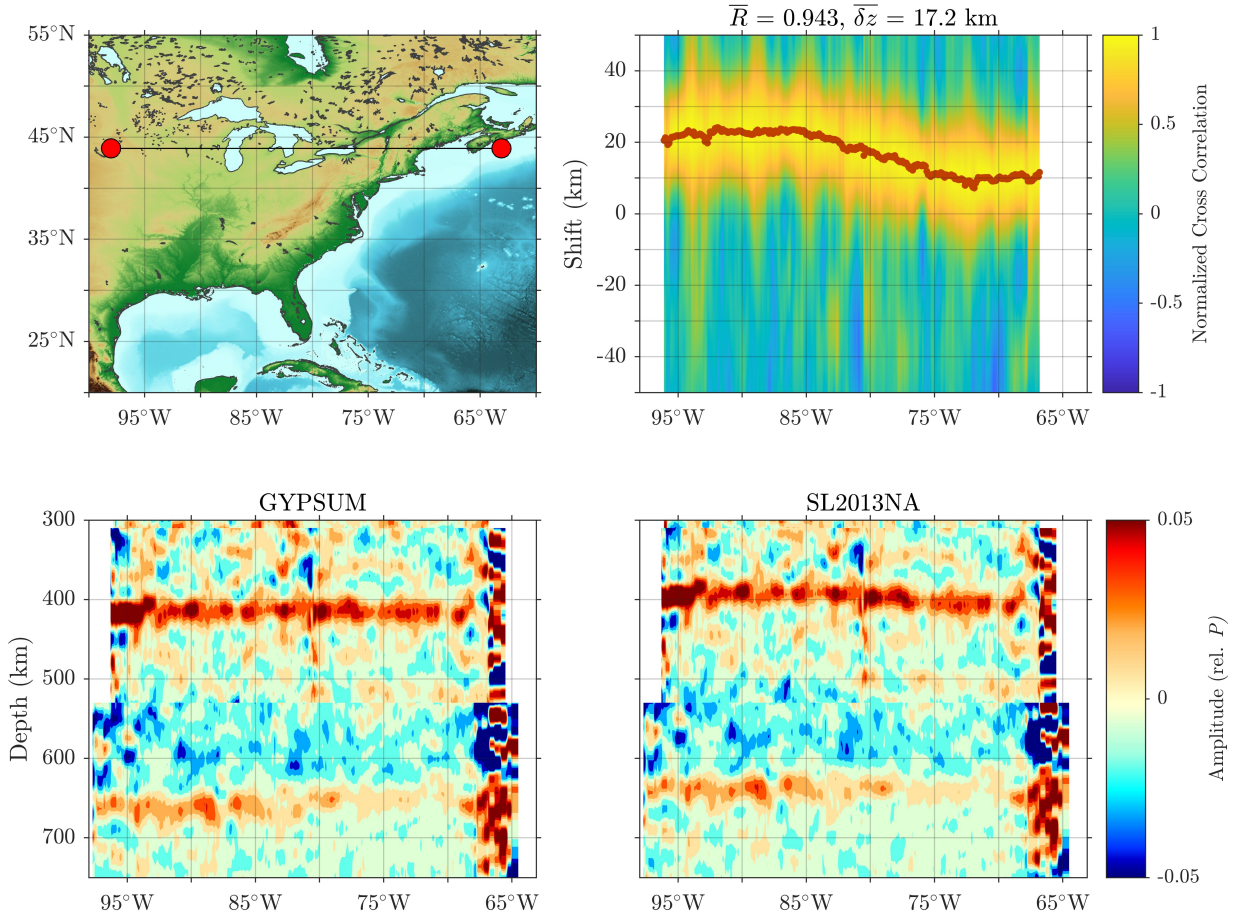

Figure S16: Same as Fig. S15 but for models GyPSuM and SL2013NA.

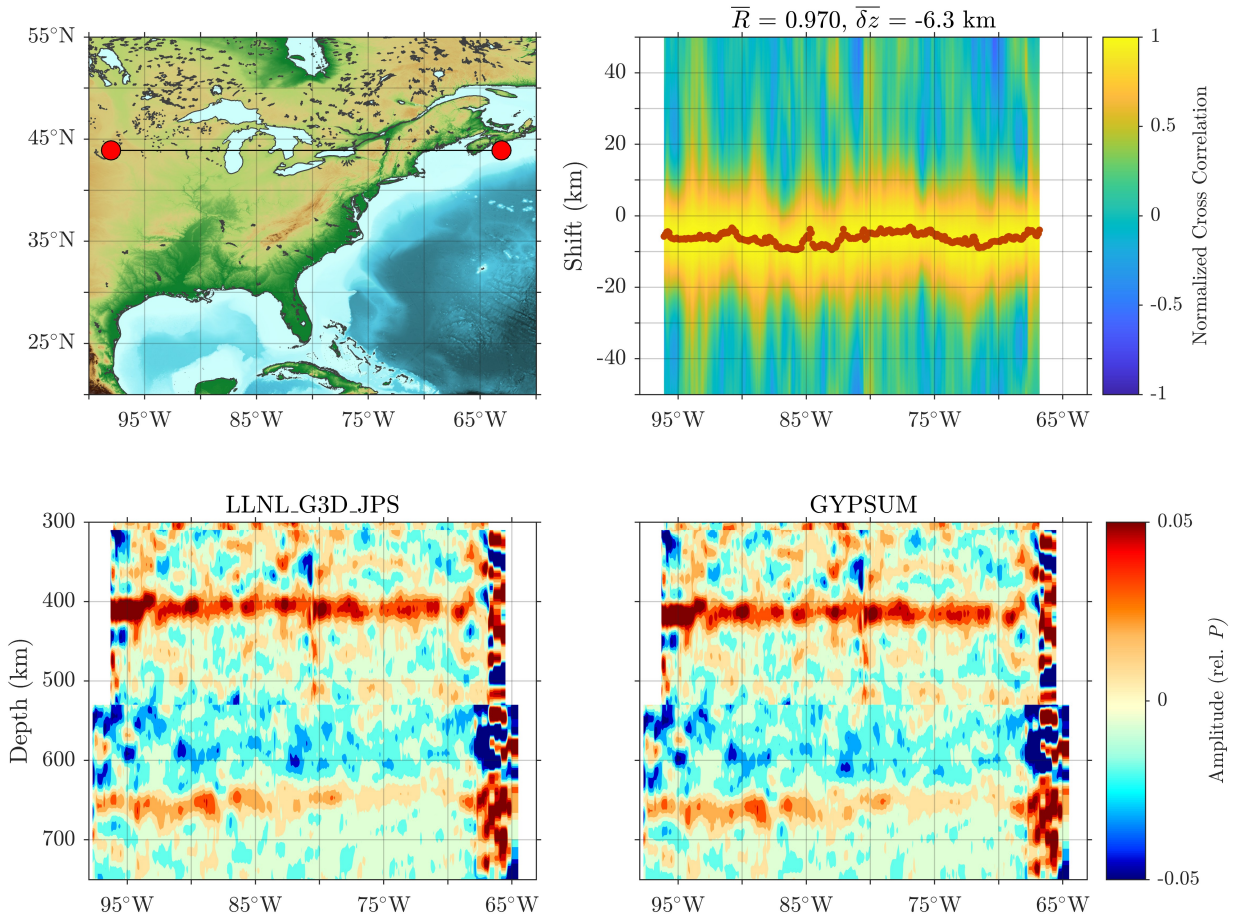

Figure S17: Same as Fig. S15 but for models LLNL_G3D_JPS and GyPSuM.

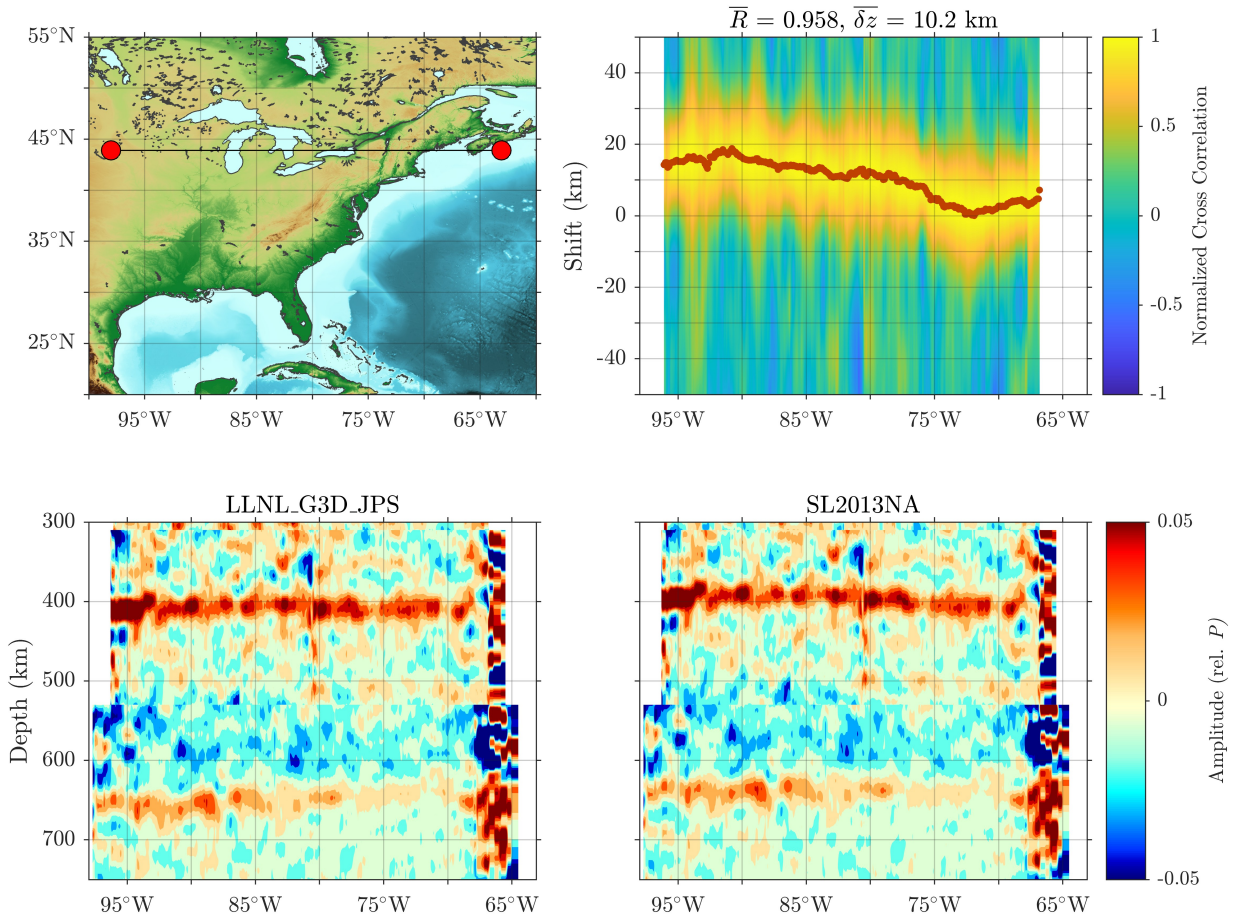

Figure S18: Same as Fig. S15 but for models LLNL_G3D_JPS and SL2013NA.

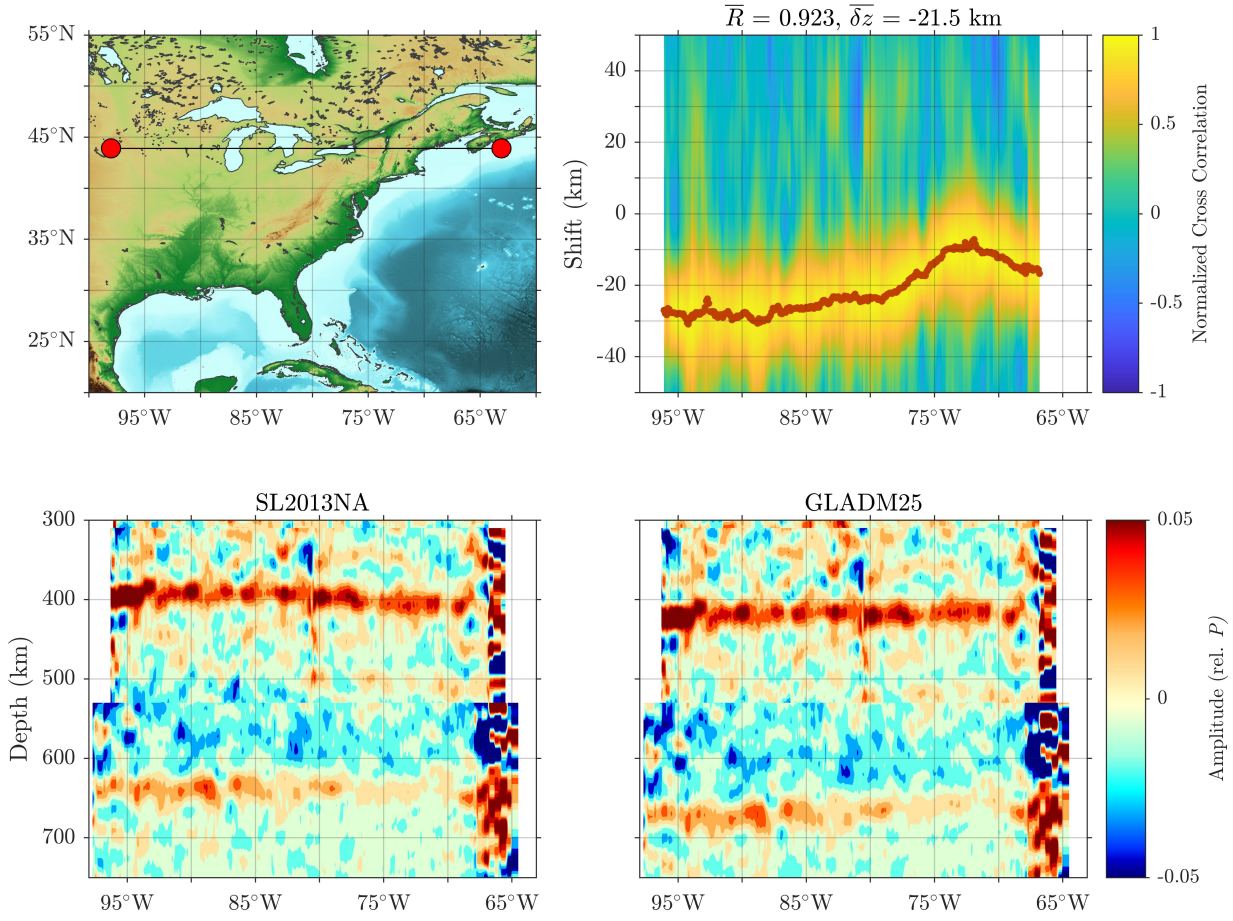

Figure S19: Same as Fig. S15 but for models SL2013NA and GLADM25.

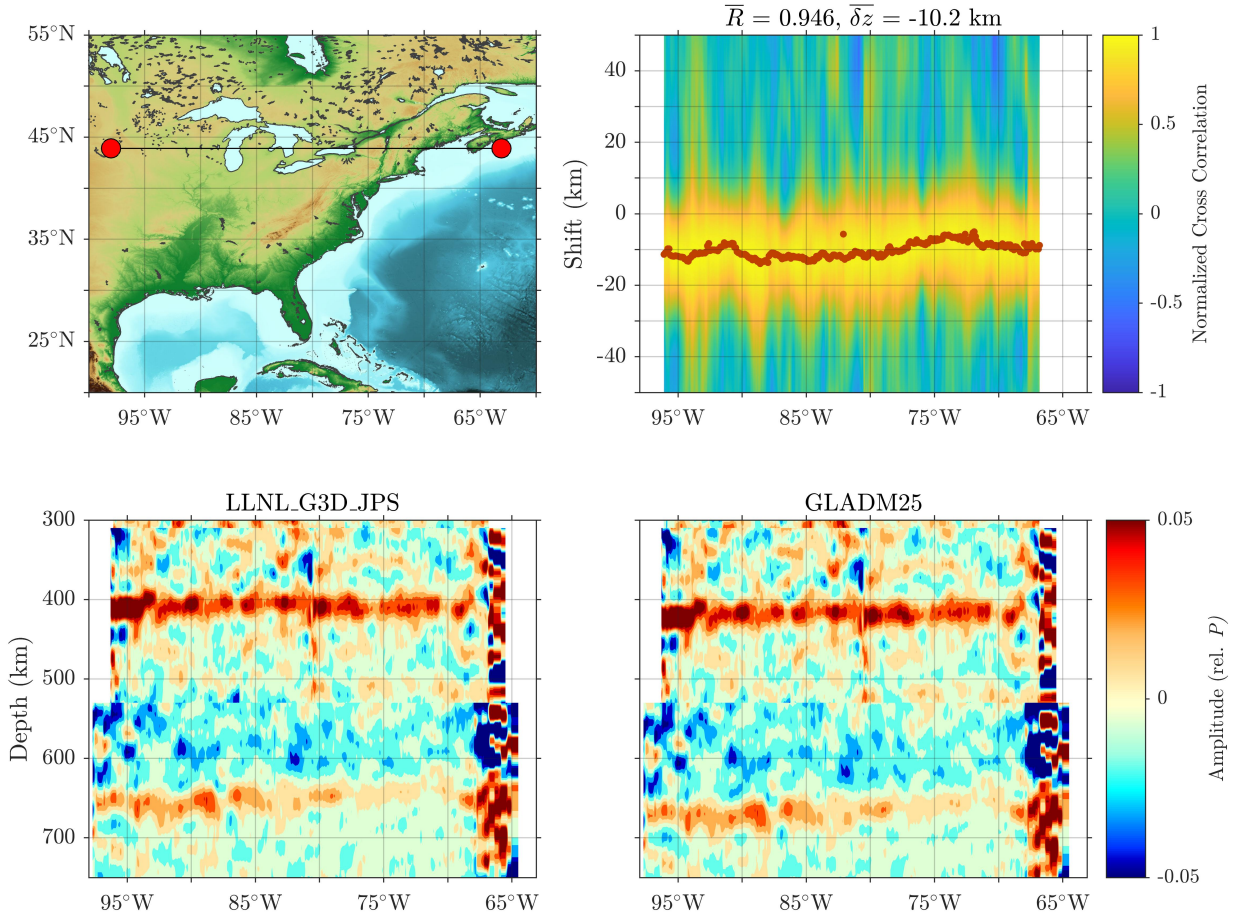

Figure S20: Same as Fig. S15 but for models LLNL_G3D_JPS and GLADM25.

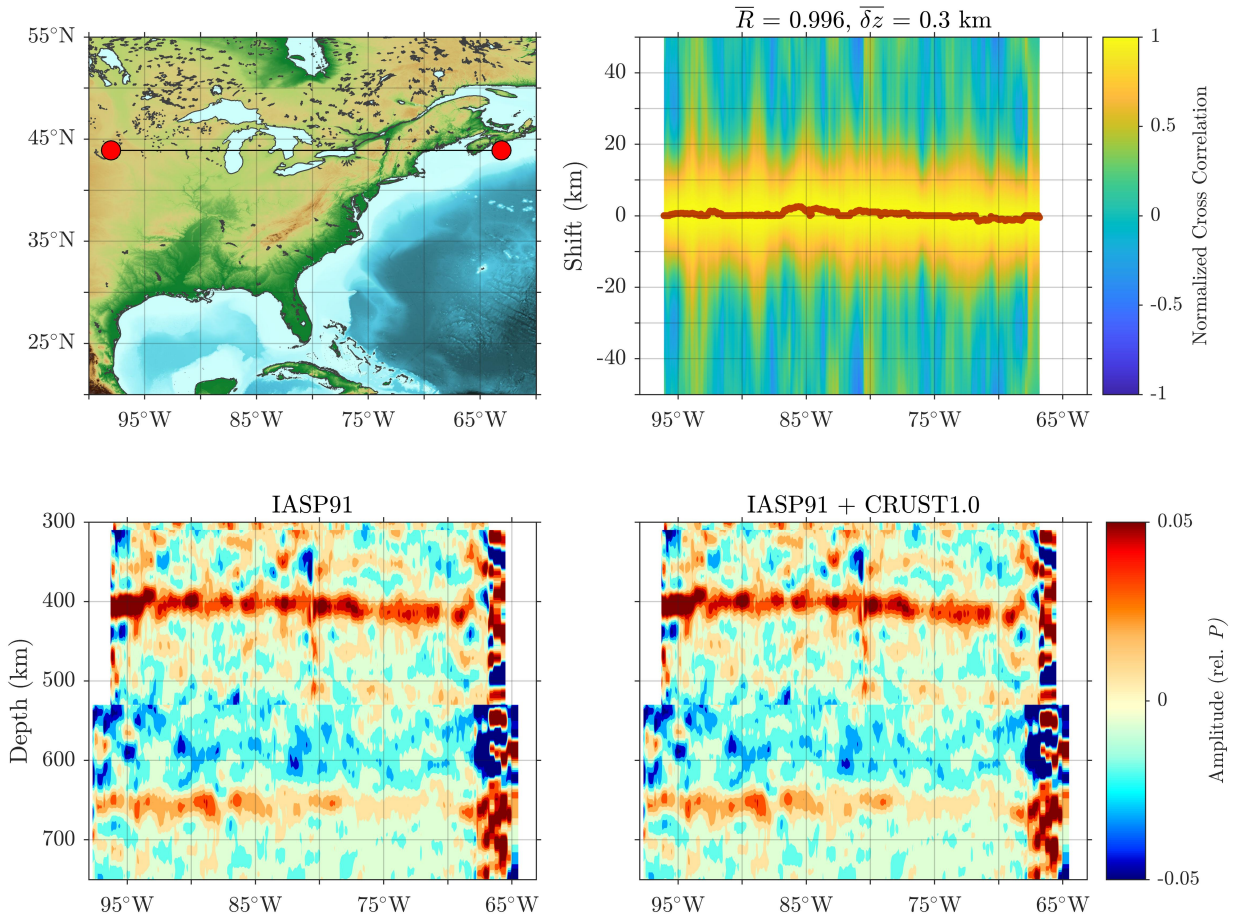

Figure S21: Same as Fig. S15 but for models IASP91 and IASP91 + CRUST1.0.

References

Lawrence, J. F., & Shearer, P. M. (2006). A global study of transition zone thickness using receiver functions. *J. Geophys. Res.*, *111*(B06), B06307, doi: 10.1029/2005JB003973.

Nissen-Meyer, T., van Driel, M., Stähler, S. C., Hosseini, K., Hempel, S., Auer, L., ... Fournier, A. (2014). AxiSEM: broadband 3-D seismic wavefields in axisymmetric media. *Solid Earth*, *5*, 425–445, doi: 10.5194/se-5-425-2014.